Modulation of Ka-Band Doppler Radar Signals Backscattered From the Sea Surface

Yury Yu. Yurovsky, Vladimir N. Kudryavtsev, Bertrand Chapron, and Semyon A. Grodsky

***Abstract*— This paper presents dual copolarized (VV and HH) Ka-band radar measurements of joint modulation of normalized radar cross section (NRCS) and Doppler velocity (DV) performed from a sea research platform. NRCS and DV modulations are well correlated. NRCS modulations exhibit a spiky structure. HH modulations are stronger than VV ones leading to modulations of the polarization ratio. This suggests that an important portion of NRCS modulations is produced by nonpolarized radar returns from modulated wave breaking facets. DV modulations reveal that at incidence angles <50°, NRCS spikes are attributable to rather slow moving facets, which may be interpreted as short wave breaking disturbances embedded in the water at crests of modulating waves. Using the DV as a proxy for wave gauge, a modulation transfer function (MTF) is estimated for both polarizations. The hydrodynamics component of the total MTF, hydro-MTF, combines NRCS modulations supported by Bragg waves and wave breaking. The contribution of each type of facets to the hydro-MTF is weighted by its partial contribution to the NRCS, and thus, hydro-MTF becomes dependent on radar polarization. Using hydro-MTF for HH and VV, Bragg wave and wave breaking modulations are separated. Wave breaking modulations are significant, with MTF amplitude varying from 5 to about 30 depending on wind speed. Ka-band Bragg waves are strongly modulated at low winds, but their modulation almost vanishes at moderate winds. Finally, we propose an empirical MTF parameterization based on polynomial fitting as a function of observation geometry and wind.**

***Index Terms*— Doppler shift, modulation transfer function (MTF), radar backscattering, sea surface, spikes, wave breaking.**

I. INTRODUCTION

OCEAN radar backscattering is modulated by surface waves due to wave-induced modulations of surface slopes (tilt modulation) and roughness (hydrodynamics modulation). Phase modulations of radar backscattering, i.e., Doppler frequency shifts, are governed by local line-of-sight (LOS) velocity, and thus are also modulated by surface wave orbital velocities. Unresolved, likely modulated, waves with wavelengths shorter than the radar footprint are inherently averaged and contribute to the time mean normalized radar cross section (NRCS) and Doppler velocity (DV). Correlated components of DV and NRCS explain the observed C-band Doppler centroid anomalies present even in the absence of currents [1], [2]. Higher frequency radar technique, including Ku-band measurements [3], Ka-band DopplerScat [4], and Sea surface KInematics Multiscale monitoring [5] build on the combined measurements of NRCS and DV, are aimed to provide new global satellite oceanographic products, such as surface currents.

Ocean Ka-band measurements of joint modulation of NRCS and DV are still rare. Early Ka-band measurements have been collected during NORDSEE platform experiments [6], [7]. An impact of waves on radar backscattering modulation is normally described in terms of a complex modulation transfer function (MTF) [8], whose experimental estimates are available from tower-based and air/space-borne sensors [6], [7], [9]–[13]. A theoretical explanation of the observed MTF is generally based on the relaxation approximation for Bragg waves [14]. But, this approximation results in an unrealistically fast decrease of MTF magnitude with a radar frequency. An effect of wind stress modulation by long waves (LWs) has been proposed to explain the observed magnitude of MTF [12], [15]. However, too strong wind stress modulations are required in order to explain the observations. As shown in [16] and [17], the effect of wave breaking is necessary to explain the time mean and modulation properties of both NRCS and DV.

In this paper, we further report the results of multiyear platform-based Ka-band radar measurements. Following the analysis of a time mean NRCS [18], the present effort focuses on the modulation properties of NRCS and DV. To estimate these properties, we rely on the potential ability of a Doppler radar to act as a wave gauge [8]. To improve this approach, we introduce a correction function associated with a radar DV response to LW orbital velocity. Derived dual copolarized (VV and HH) MTF estimates are fit by empirical polynomials. Similar to "Bragg-non-Bragg" decomposition of NRCS [19], the empirical dual copolarized MTF is decomposed in order to separate the hydrodynamics MTF for Bragg roughness and non-Bragg scatterers (wave breaking).

II. EXPERIMENT, DATA, AND METHODS

The measurements were performed from the Black Sea research platform during 2009–2015 using a 37.5-GHz

Manuscript received August 6, 2017; revised November 30, 2017; accepted December 19, 2017. The core support of the work was provided by Russian Science Foundation under Grant 15-17-20020. Field experiments in 2014–2015 were supported by FASO of Russia under the State Assignment 0827-2014-0010. At the final stage, this work was supported in part by the National Aeronautics and Space Administration under Grant NNX15AG40G and in part by the Ministry of Science and Education via Goszadanie 5.2928.2017/PP. *(Corresponding author: Yury Yu. Yurovsky.)*

Yu. Yu. Yurovsky is with the Federal State Budget Scientific Institution "Marine Hydrophysical Institute of RAS," 299011 Sevastopol, Russia (e-mail: yyyurovsky@gmail.com).

V. N. Kudryavtsev is with the Federal State Budget Scientific Institution "Marine Hydrophysical Institute of RAS," 299011 Sevastopol, Russia, and also with the Satellite Oceanography Laboratory, Russian State Hydrometeorological University, 195196 Saint Petersburg, Russia (e-mail: kudr@rshu.ru).

B. Chapron is with the Institut Français de Recherche pour l'Exploitation de la Mer, 29280 Plouzané, France (e-mail: bertrand.chapron@ifremer.fr).

S. A. Grodsky is with the Department of Atmospheric and Oceanic Science, University of Maryland, College Park, MD 20742, USA (e-mail: senya@umd.edu).

Color versions of one or more of the figures in this paper are available online at http://ieeexplore.ieee.org.

Digital Object Identifier 10.1109/TGRS.2017.2787459

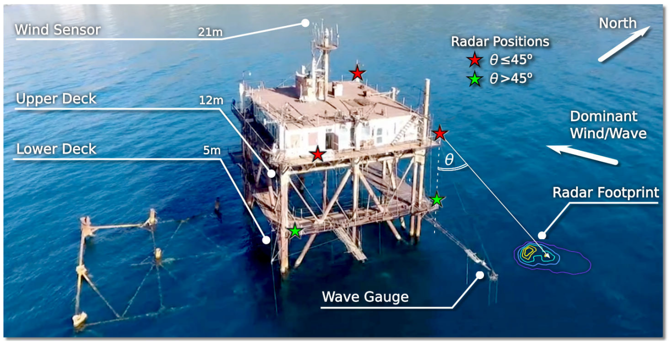

Fig. 1. Black Sea research platform (44°23′35″N, 33°59′04″E). Wrecks to the left are remains of another platform destroyed by storms. This south-west azimuth sector is not used for measurements.

continuous-wave dual copolarized Doppler Ka-band radar that operated in the hybrid polarization mode with a slant (45°) transmit polarization plane and two receiving channels for vertical and horizontal polarizations. Most of the data and instrumentations used in this paper are similar to those described in [18]. This configuration implies a cross-polarization contamination of received signals, which, however, is weak for our conditions and is disregarded (see [18, Appendix] for more details).

The radar was installed at different platform locations (heights) depending on desired radar-to-wave azimuth ϕ and incidence angle θ (see Fig. 1). To keep a reliable balance between radar footprint size, signal-to-noise ratio, and antenna far-field applicability distance (>6 m), the acquisitions were made from either the upper (12 m height) or the lower (6 m height) platform decks for $\theta \leq 45°$ or $\theta > 45°$, respectively. The correction for a radar antenna pattern is discussed in Appendix A.

Supplementary meteorological measurements were made using the Davis Vantage Pro station with air sensors mounted at 21 m height. Neutral 10-m wind speed U was calculated using the COARE3.0 algorithm [20]. Surface wave elevations were recorded by six-wire wave gauge antenna (five strings in the corners of a pentagon and one in its center, each pair separated by about 25 cm) installed from 11-m horizontal stern. The distance between wave gauge and radar footprint varied from a few meters to tens of meters, which did not allow for phase comparison between radar and wave elevation signals.

Directional surface wave spectra were estimated over 30-min intervals by the maximum-likelihood method (DIWASP package [21]), from which the wave peak frequency f_p and its direction ϕ_p were estimated. Complex situations with short offshore fetches, strong swell, and multiple swell peaks were eliminated from the analysis. Only records with coaligned wind and waves were included, while records with wind and wave directions deviating by >30° were not included. For the included records, radar-to-wind and radar-to-wave azimuths were assumed equal (radar-to-wave azimuth was used by default). Throughout the text, the following azimuth notations are used: $\phi = 0°$—upwind, $\phi = 90°$—crosswind, and $\phi = 180°$—downwind.

Doppler measurements performed from a static platform allow to detect both the instantaneous (centroid of the instantaneous Doppler spectrum) and the NRCS-weighted (centroid of the time-mean Doppler spectrum) Doppler shifts, and thus distinguish between the mean scatterer velocity and the wave-induced contribution.

The raw radar data processing followed [22]. In-phase $I(t)$ quadrature $Q(t)$ signal components were digitized at 40-kHz rate for VV and HH polarizations, from which instantaneous Doppler spectra were computed over consecutive $\tau = 0.2$ s intervals

$$S(\nu, t) = \overline{\left| \int_{t-\tau/2}^{t+\tau/2} (I + iQ) e^{-i2\pi\nu t} dt \right|^2} \tag{1}$$

where $\overline{(\ldots)}$ stands for ensemble averaging with two degrees of freedom, and ν is the Doppler frequency. Instantaneous NRCS $\sigma(t) = \int S(\nu, t) d\nu$, Doppler frequency shift $f_D(t) = \int \nu S(\nu, t) d\nu / \sigma(t)$, and Doppler bandwidth (DW) $\omega_D(t) = \int (\nu - f_D(t))^2 \, S(\nu, t) d\nu / \sigma(t)$ were estimated as corresponding momenta of the instantaneous Doppler spectrum $S(t, \nu)$. Instantaneous Doppler frequency shift $f_D(t)$ translates into instantaneous LOS DV, $v(t) = \pi k_r^{-1} f_D(t)$, where k_r is the radar wavenumber.

The original radar records were subdivided into 5-min samples. The total number of analyzed samples is about 500. Data distribution versus incidence angle θ radar-to-wave azimuth ϕ, and wind speed U is shown in Fig. 2. The absence of data at low winds ($U <$ 3–4 m/s) is due to low signal-to-noise ratio under these conditions. The majority of the data are collected at moderate winds, $U =$ 8–12 m/s. Downwind radar orientations are rare because of platform shadowing.

III. RADAR SIGNAL FEATURES

A. Time Series

Time series of running VV and HH Doppler spectra (computed over consecutive 0.2-s intervals, see Fig. 3) show a marked modulation certainly associated with long surface waves with a period of about 4 s. The spatial scale resolved by a radar is determined by its ground footprint size. The latter depends on the incidence angle and in our case may vary by a few meters (see Appendix A for more details). We refer to these resolved waves as LWs.

Fig. 3 reveals the occurrence of radar signal spikes also linked to local maxima of the Doppler frequency shift. From visual observations, these spikes are usually associated with breaker passages within the radar footprint. Note also that NRCS spikes are not accompanied by noticeable DV spikes, at least at $\theta \approx 53°$ and $U = 10$ m/s. This suggests that measured NRCS spikes do not necessarily correspond to "fast moving" scatterers, but rather slow moving very rough surface elements with the translation speed somewhat higher than the LW orbital velocity. Fig. 3 also shows that the Doppler spectrum bandwidth (DW) correlates well with the DV. This indicates that the spread of radar scatterer velocities increases in areas, where the DV has local maxima (wave crests for upwind observation geometry in Fig. 3). In other words, the scatterers in rough areas associated with breaking waves do not move as "frozen" targets, but have rather wide speed distribution.

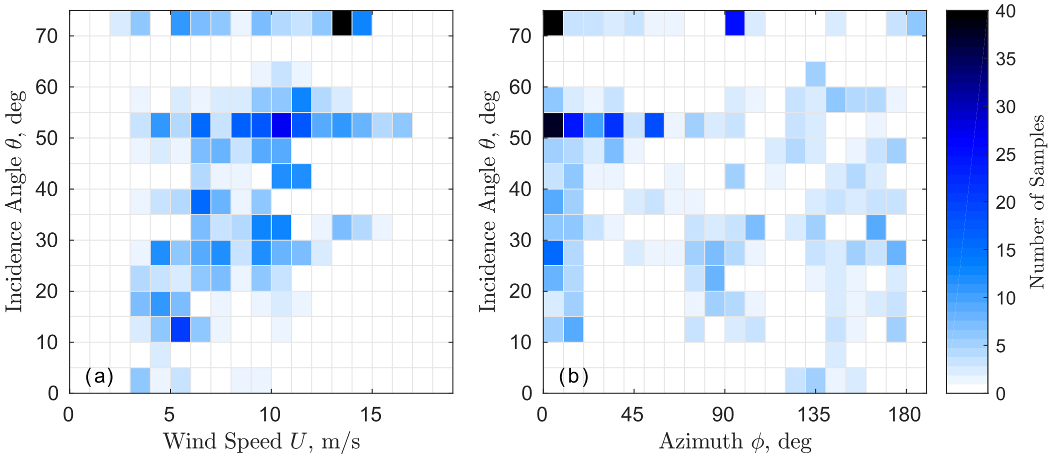

Fig. 2. Data set statistics. Number of data samples versus (a) incidence angle θ and wind speed U and (b) incidence angle θ and radar-to-wind/wave azimuth ϕ.

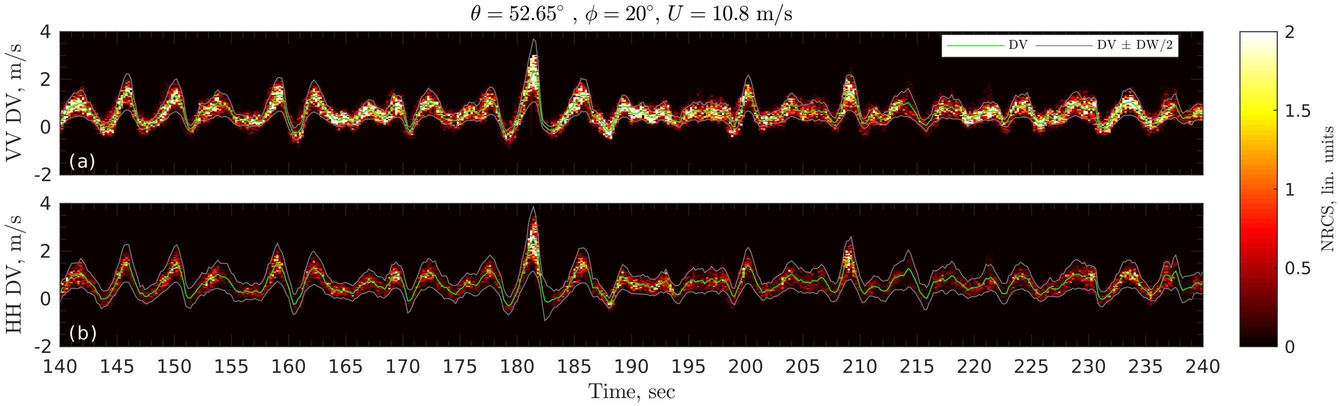

Fig. 3. Example of instantaneous (a) VV and (b) HH Doppler spectra ($\theta \approx 53°$, upwind, and $U = 10$ m/s) as a function of time. DV (green, middle line) and Doppler spectrum width (gray, top and bottom lines) are shown. Color shades correspond to spectrum density.

As was first suggested in [8], the Doppler signal can be used for the direct estimation of LW orbital velocities, and thus, after integration, LW surface displacements and tilts. Assuming that DV fluctuations are solely produced by LW orbital velocities, the relationship between Fourier harmonics of wave elevation $\hat{\xi}$ and DV $\hat{v}$ can be written as [8], [23]

$$\hat{v}(\omega) = \omega G(\theta, \phi)\hat{\xi}(\omega) \tag{2}$$

$$G(\theta, \phi) = \cos\phi \sin\theta + i\cos\theta \tag{3}$$

where ω is the LW frequency, θ is the incidence angle ϕ is the radar-to-wave azimuth, G is the geometric transformation coefficient projecting the wave orbital velocity onto the radar LOS direction, and hat above any quantity denotes its Fourier transform. In this paper, we ignore the shallow water effects. During the experiments, LW wavenumbers were in the range $k > 0.1$ rad/m, that for water depth $D = 25$ m gives $kD > 2.5$.

NRCS modulations by LWs are described in terms of the radar MTF

$$M = \frac{\hat{\sigma}}{\overline{\sigma} k \hat{\xi}} \tag{4}$$

where k is the LW wavenumber linked to ω by the deep water dispersion relationship, $\omega^2 = gk$, g is the gravity acceleration, $\overline{\sigma}$ is the mean (averaged over LW phase) NRCS, and $\hat{\sigma}$ is the Fourier transform of NRCS modulations by the LW with amplitude ξ. By definition, the MTF describes a linear relationship between wave slopes ($k\hat{\xi}$) and relative NRCS variations ($\hat{\sigma}/\overline{\sigma}$), which must be small. Although in our case the latter requirement is not always the case, we accept the linear MTF concept for comparability with the previous studies (see [6], [8], [23], and others).

Using (2) and (3), the MTF (4) can be calculated from Doppler radar measurements as

$$M = \frac{g G S_{\sigma v}}{\overline{\sigma} \omega S_{vv}} \tag{5}$$

where $S_{\sigma v}$ is the cross spectrum between NRCS and DV time series and S_{vv} is the autospectrum of DV time series.

Besides dependences on LW tilt and roughness modulations, a platform-based NRCS also depends on wave-induced changes in range and footprint area. For the beam-limited footprint, the range dependence is proportional to R^{-2} (see [23, eq. (45)]), while the footprint area varies as $\cos(k\xi)$. The range and footprint area modulations were removed from the received power using instantaneous range and LW tilt modulations derived from the measured DV [see (2) and (3)].

Sample time series of NRCS, polarization ratio (PR), $\mathrm{PR} = \sigma^{\mathrm{vv}}/\sigma^{\mathrm{hh}}$, and DV are shown in Fig. 4 together with LW elevation ξ and slope ζ computed from VV DV using

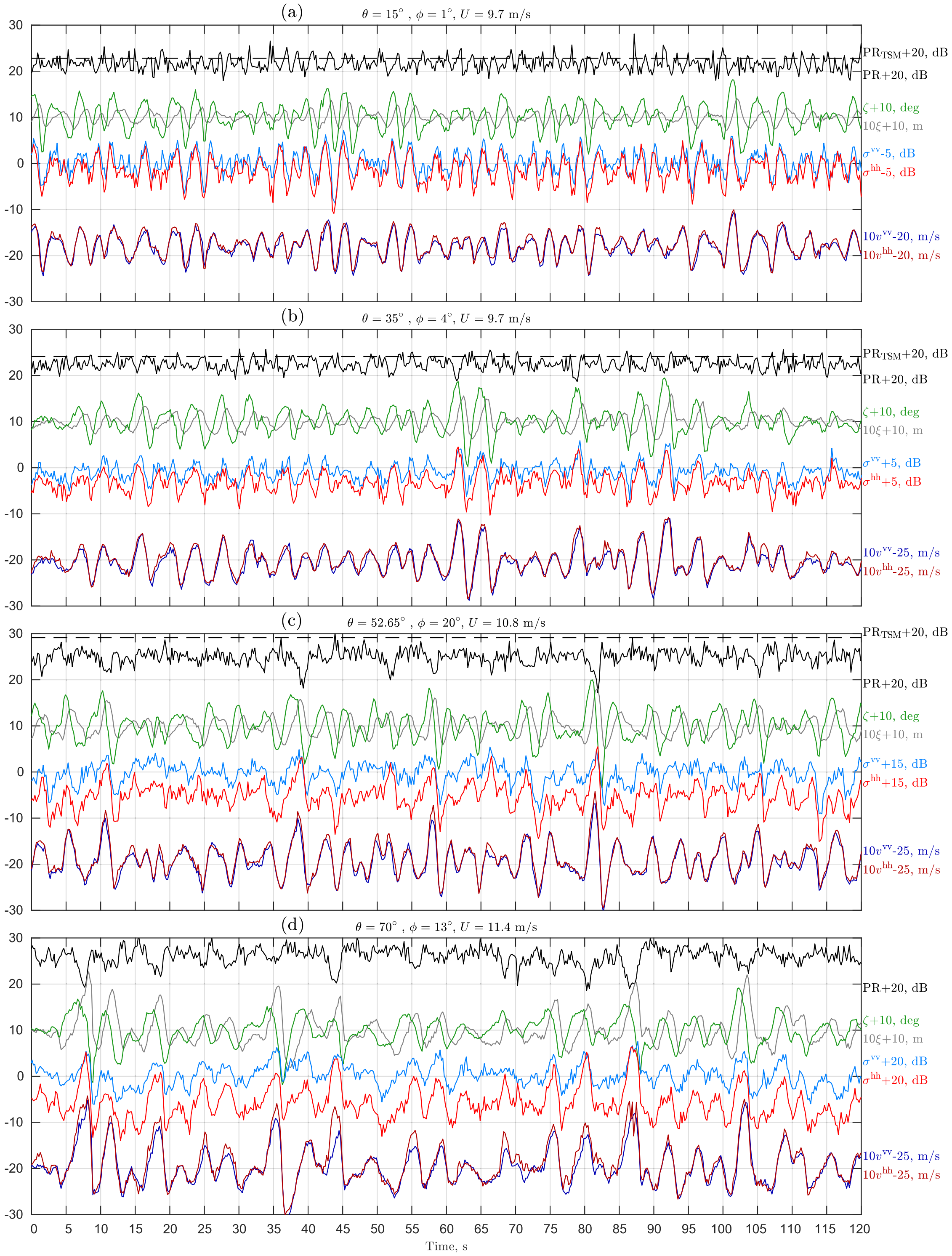

Fig. 4. Time series of NRCS (σ^{VV}—red line and σ^{hh}—blue line), DV (υ^{VV}—red dark line and υ^{hh}—blue dark line), PR (PR—black solid line), wave elevation (ξ—gray line), and wave slope (ζ—green line) inferred from VV DV. Theoretical Two-Scale Model (TSM) PR is shown by horizontal black dashed lines (for $\theta = 70^\circ$, TSM PR is out of scale). The signals are shifted along the y-axis for better visibility. (a) $\theta = 15^\circ$, $\phi = 1^\circ$, and $U = 9.7$ m/s. (b) $\theta = 35^\circ$, $\phi = 4^\circ$, and $U = 9.7$ m/s. (c) $\theta = 52.65^\circ$, $\phi = 20^\circ$, and $U = 10.8$ m/s. (d) $\theta = 70^\circ$, $\phi = 13^\circ$, and $U = 11.4$ m/s.

(2) and (3). Both VV and HH NRCS are well correlated with LW elevations and slopes derived from DV measurements. At low incidence angles $\theta = 15^\circ$ and 35°, the NRCS is enhanced on forward LW slopes suggesting the dominant role of the tilt modulation mechanism. At larger θ, the relative importance of the tilt modulation decreases and the maximum of NRCS modulation shifts toward LW crests and approximately follows wave elevations. This reflects a major contribution of the hydrodynamics modulation to the total MTF.

The measured PR is systematically lower than the PR predicted by a standard Two-Scale Model (TSM, see Appendix B for its evaluation details). A remarkable feature in Fig. 4

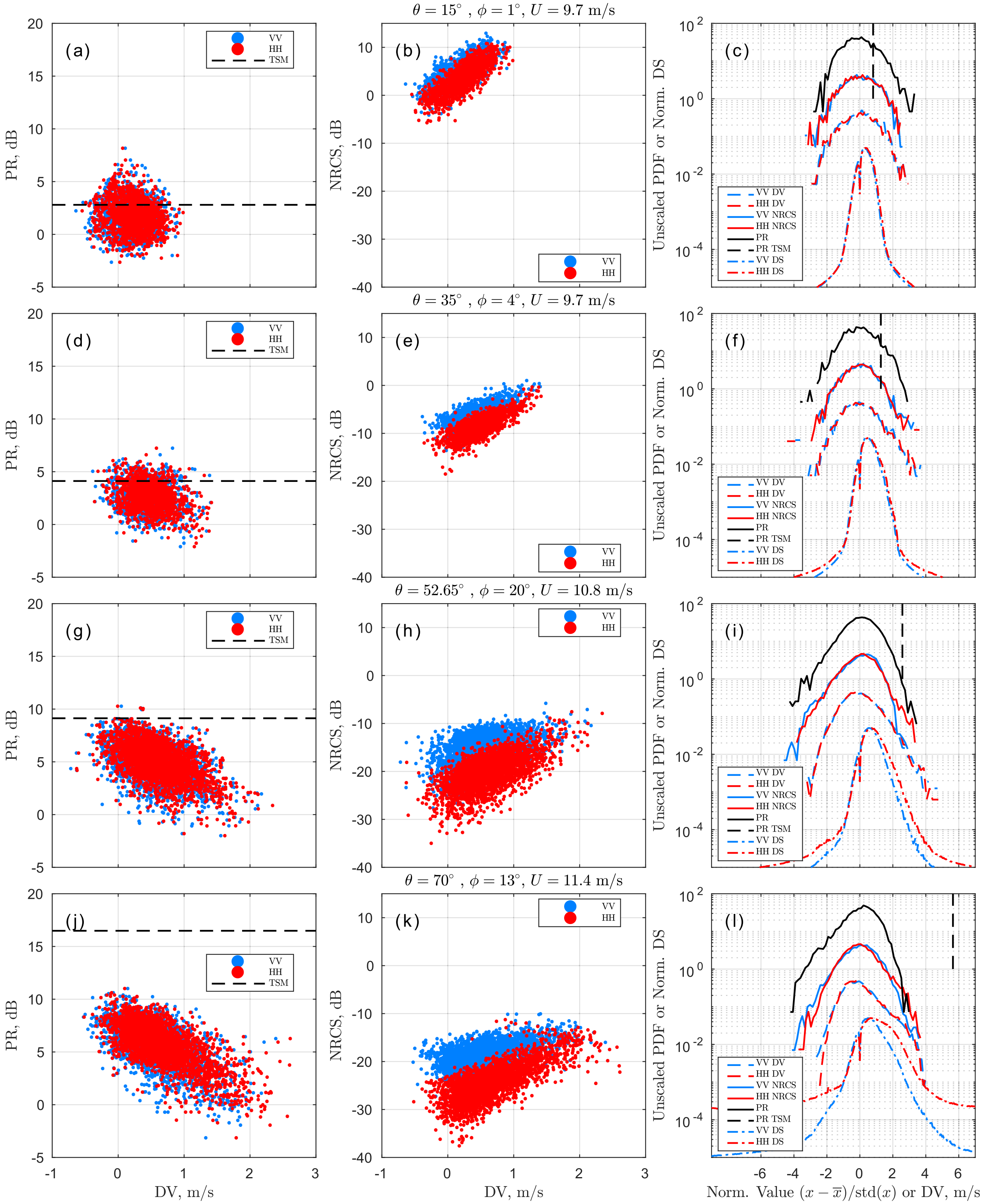

Fig. 5. Scatter plots of (left) instantaneous PR *versus* DV and (middle) NRCS versus DV. (Right column) Unscaled pdfs of centered PR, NRCS, DV, and unscaled Doppler spectra (DS, the x-axis for Doppler spectra is DV in m/s). The rows correspond to the time series shown in Fig. 4. (a)–(c) $\theta = 15°$, $\phi = 1°$, and $U = 9.7$ m/s. (d)–(f) $\theta = 35°$, $\phi = 4°$, and $U = 9.7$ m/s. (g)–(i) $\theta = 52.65°$, $\phi = 20°$, and $U = 10.8$ m/s. (j)–(l) $\theta = 70°$, $\phi = 13°$, and $U = 11.4$ m/s.

is an apparent correlation between strong NRCS peaks and PR drops. For some of large NRCS peaks, the PR drops down to 0 dB indicating that NRCS peaks are nonpolarized, $\sigma^{\mathrm{vv}} = \sigma^{\mathrm{hh}}$. Enhanced NRCS peaks presumably represent nonpolarized (NP) radar returns from steep and rough surface patterns related to breaking waves (see Fig. 4(b) at $t = 62$ s, (c) at $t = 82$ s, and (d) at $t = 87$ s). Excepting cases of HH backscattering at high incidence angles ($\theta = 70°$), the DV exhibits quite smooth behavior with modulations comparable with LW orbital velocities (see also Fig. 7). A notable feature is that strong NRCS peaks are not accompanied by remarkable DV "spikes." This suggests that, at our observation geometry,

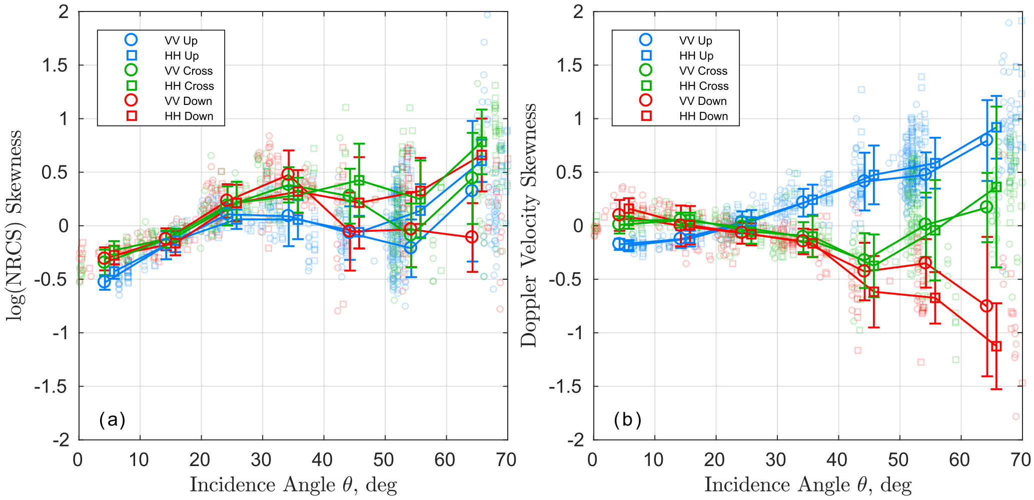

Fig. 6. Skewness of instantaneous (a) NRCS in logarithmic units, (b) DV (circles are VV, squares are HH, blue line is upwind, green line is crosswind, and red line is downwind) versus incidence angle for all conditions.

wave breaking enhancement on the crests of LWs does not lead to DV anomalies apparently deviating from LW orbital velocities.

B. Distributions, Skewness, and Doppler Spectra

Scatter plots "NRCS versus DV" and "PR versus DV" corresponding to the time series in Fig. 4 are presented in the left and middle columns of Fig. 5. The most apparent feature is the positive correlation between DV and NRCS variations reflecting NRCS enhancement on forward slopes close to wave crests, where DV has maximum positive values for the upwind observation geometry. At $\theta > 50°$, PR and DV variations are negatively correlated [see Fig. 5(g) and (j)] suggesting that NP backscattering from modulated breaking waves does contribute at these incidence angles.

The centered probability density functions [pdfs, Fig. 5 (right column)] provide a deeper insight into specific features of joint modulations of NRCS and DV. First, the distribution of DV is quite symmetrical relative to its mean value, while the distribution of either VV or HH NRCS as well as PR (all plotted in logarithmic scale) is strongly skewed (if converted to a linear scale). This shows that enhancements of NRCS in the areas of positive DV (wave crests for upwind observations) are much stronger than its suppressions in the areas of negative DV. The skewness of NRCS, PR, and DV pdfs becomes more pronounced at large θ [see Fig. 5(i) and (l)]. Interestingly, that distribution of DV and log(NRCS) is inversely skewed for this particular observation geometry. DV pdf has a positive "tail" corresponding to fast breakers moving toward an upwind looking radar. The negative "tail" of log(NRCS) pdf is explained by signal drops (pauses) over turbulent patches following wave breaking events.

Doppler spectra [see Fig. 5 (right column)] exhibit features similar to those present in DV pdfs. In particular, the tail corresponding to positive DVs becomes more pronounced at large θ. This is better seen in HH Doppler spectrum at $\theta = 70°$ [see Fig. 5(l)], which has a rather broad peak area extending into positive DVs of about 2.5 m/s. This is in line with previous observations (see [24]–[26]) that have been attributed to "fast scatterers" associated with breaking waves. The similarity between DV pdfs and Doppler spectra allows using the skewness of DV pdf as a measure of Doppler spectrum asymmetry and corresponding fast scatterer impact.

The skewness characteristics for different observation geometries are shown in Fig. 6. The log(NRCS) skewness is near zero at $\theta \approx 20°$ and grows rapidly with increasing θ from ≈ -0.5 near the nadir to ≈ 0.5 at $\theta = 70°$. Interestingly, this growth is not regular. There is a local maximum at $\theta = 30°$–$35°$, which is more pronounced for VV polarization. This maximum can be associated with a local maximum in the gradient of the tilt-MTF, $\partial^2\sigma/\partial\theta^2$, that leads to nonlinear NRCS modulation. At $\theta > 55°$, the skewness grows again due to the contribution of strong positive spikes from wave breaking that is more prominent at HH than at VV polarization. The skewness of DV increases in magnitude with the incidence angle. Its sign is azimuth dependent reflecting the relative direction of fast moving breakers.

IV. RELATION OF DV OSCILLATIONS TO LW ORBITAL MOTIONS AND WAVE BREAKING MODULATIONS

A. DV-Derived Elevation Spectra

When DV is used as a proxy for wave gauge, it is usually assumed that DV oscillations are produced solely by the orbital motions [23], while other mechanisms of DV modulations (e.g., by wave breaking) are disregarded. To account for these latter mechanisms, a DV response function defined as the ratio between the measured DV spectrum and its expected value from the linear wave theory is introduced

$$\mu = \frac{S_{vv}}{|G|^2\omega^2 S_{\xi\xi}} \tag{6}$$

where S_{vv} is the DV spectrum corrected for the effect of footprint filtering (see (20) in Appendix A).

Using this definition, the DV variation (2) is modified as

$$\hat{v} = \mu^{1/2} G\omega\hat{\xi}. \tag{7}$$

The spectral shape of the response function μ is evaluated from wave gauge measurements (see Fig. 7). The latter is

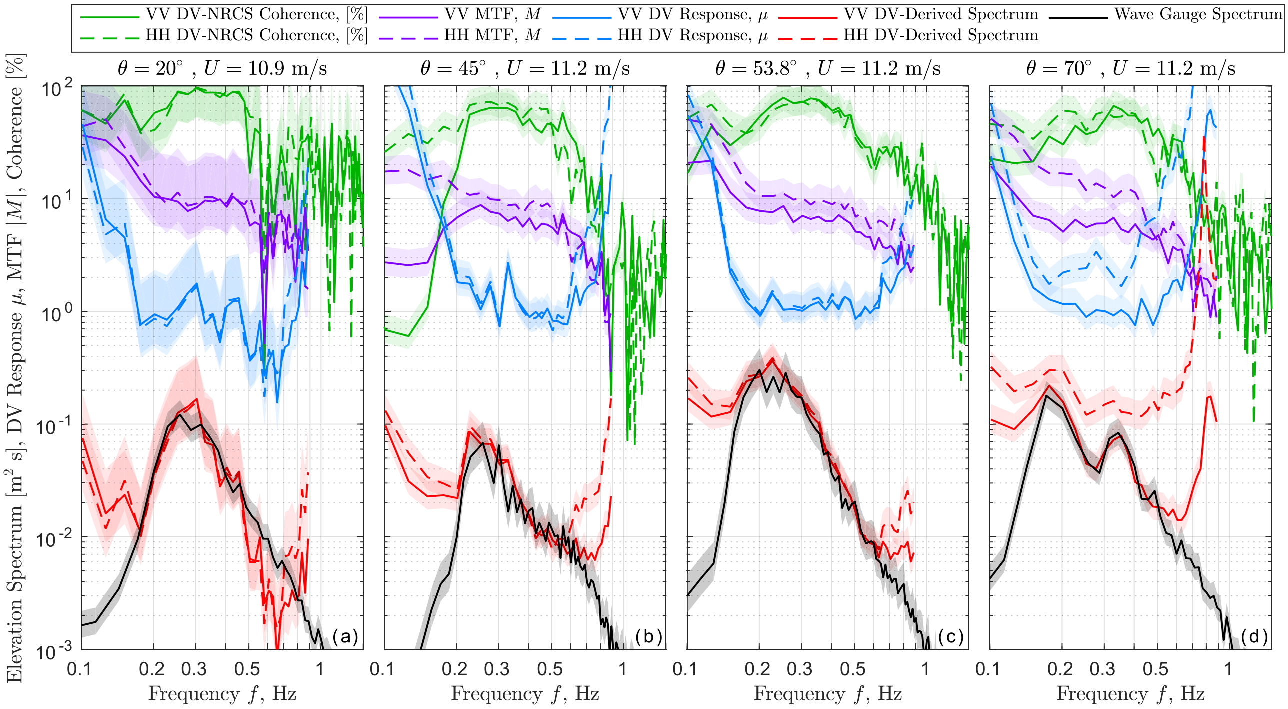

Fig. 7. Upwind coherence between DV and NRCS, MTF (M), DV response function (μ), DV-derived elevation spectra, and wave gauge elevation spectra for (a) $\theta = 20°$, (b) $\theta = 45°$, (c) $\theta = 53.8°$, and (d) $\theta = 70°$. DV-derived spectra are corrected for the radar footprint response function [see (20)].

neither contemporaneous in time nor collocated in space with the radar time series. Therefore, only autospectra of DV and LW parameters can be jointly analyzed.

Typical wave gauge frequency elevation spectra and elevation spectra derived from DV measurements

$$S_{\xi\xi} = |G|^{-2}\omega^{-2}S_{vv} \tag{8}$$

demonstrate rather good agreement especially in the vicinity of their spectral peaks. As already discussed, such agreement is not expected given the significant impact of wave breaking modulations on radar signal modulations (see Figs. 4 and 5). But, no remarkable difference between DV spectrum level and that derived from wave gauge data can be revealed in the spectrum peak area at low to moderate θ [see Fig. 7(a)–(c)]. A noticeable excess appears only at large incidence angles $\theta = 70°$ and HH polarization [see Fig. 7(d)].

The DV response function is close to 1 between the wave peak frequency f_p and the radar pattern (RP) cutoff frequency f_{cut}. At $f > f_{\text{cut}}$, its magnitude rapidly increases, while DV-NRCS coherence almost vanishes (see Appendix A for details on f_{cut} estimation). Below f_p, the DV response function is also increases indicating nonnegligible low-frequency DV fluctuations probably caused either by wave groups, wind speed variations, or other modulation mechanisms which examination is out of the scope of this paper.

Assuming that μ is frequency independent, it is averaged over $f_p < f < f_{\text{cut}}$. For each data sample, the resulting averaged DV response magnitude is used to correct the orbital velocity autospectrum [S_{vv} in (9)]. The mean DV response magnitude (see Fig. 8) also illuminates the role of DV spikes associated with fast scatterers. One can note that μ increases in the crosswind direction. Probably, this increase results from uncertainties in the wave azimuth estimation. In the crosswind azimuth sector, even small errors in $|G|^2$-factor in the denominator of (6) leads to rather large errors in μ, especially at large θ. On the other hand, the magnitude of μ also increases at large $\theta \approx 70°$ (stronger for HH polarization than for VV polarization). This agrees with the concept of fast scatterers (wave breaking) that dominate HH return at large incidence angles.

B. Are the Breakers Fast or Slow Scatterers?

As already noticed, the remarkable deviation of observed PRs from Bragg-model values and the negative correlation between DV and PR [see Fig. 5 (left column)] suggest that NRCS peaks appearing on LW crests are associated with NP radar returns from breaking waves. In addition, a reasonably good correspondence between DV-derived and wave gauge elevation spectra suggests that breaking waves are (on average) "slow" facets, because the measured DV is not "distinguishable" from the LW orbital velocity (except for HH at $\theta = 70°$). Thus, at first glance, our observations conflict with a number of previous studies suggesting that wave breaking is fast moving facets. A few examples follow.

At low grazing angles, Seeman *et al.* [27] have observed strong X-band DV spikes (up to 7 m/s) corresponding to the phase speed of shoaling breaking wave (see their Fig. 4). In wave tank experiments with different microwave bands (from the S- to the W-band), Lamont-Smith *et al.* [28] have found that the DV of breakers produced by wave focusing corresponds well to their phase velocity (see their Fig. 4).

But in the open sea conditions, the DV of radar spikes is normally lower than the spectrum peak phase speed.

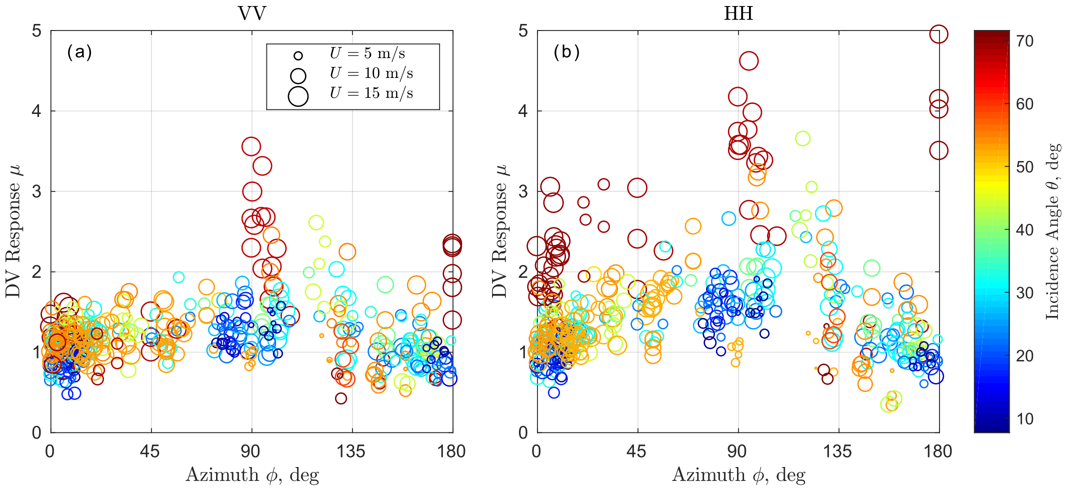

Fig. 8. DV response function μ averaged over wave frequency range $f_p < f < f_{\text{cut}}$ as a function of azimuth for (a) VV and (b) HH polarizations. Colors correspond to incidence angle, and symbol size is proportional to wind speed.

In particular, the DV of Ku-band spikes observed by Jessup *et al.* [29] at $\theta = 45°$ constituted only $\approx 25\%$ of the spectral peak phase speed. Similarly, low DV values were reported in [24] and [26] in the X-band and in [30] in the S-band at low grazing angles. Real breaking waves are distributed over a wide range of scales extending from the spectrum peak of wind generated waves to gravity waves with wavelengths of the order of 1 m. The shorter the breaking waves are the larger the surface probability breaker density produced by these waves is [31]. LWs strongly modulate breaking of shorter waves [32], and therefore, the crests of LWs (i.e., spectrum peak waves) are covered by short-scale breakers whose DV is lower than the phase speed of modulating LWs. This fact may explain the difference between DVs measured in the laboratory and open ocean conditions [33].

Nevertheless, if the DV of a short-scale breaker is equivalent to its phase velocity, a remarkable contribution of modulated breaking waves to LW-induced DV oscillations could be expected. In our measurements, such contribution is noticeable at large incidence angles and HH polarization, but it is not noticeable at smaller incidence angles (compare Fig. 7(d) with other panels in Fig. 7). This observation suggests that the DV of radar backscattering from "individual" breakers, besides LOS factor, depends on the incidence angle.

The following paradigm could justify this incidence angle dependence. A breaker originates from the explosive crest instability leading to the rapid overturning of the surface (beginning of breaker generation). Then, during its life span, an active breaker advances with the phase velocity of its carrying breaking wave, and leaves behind an expanding area of surface disturbances (enhanced surface roughness). Most likely, these disturbances are "embedded" into the water, and thus, their DVs correspond to the "water velocity." In contrast, the DV of radar backscattering from the forward slope of an active breaker corresponds to its advance velocity, and thus is close to the phase velocity of carrying breaking wave. Thus, at large incidence angles and in the upwind direction, a radar detects breakers as fast facets. At moderate incidence angles, most of the radar backscattering is produced by the enhanced roughness on the top of breakers (due to larger than forward face area), which are thus detected as slow facets.

Such paradigm may explain the observed Doppler features in a wide range of incidence angles. At any incidence angle, the incoherent NRCS of "individual" breakers is much higher than the ambient NRCS produced by resonant Bragg scattering. As a result of such NP contribution, the NRCS peaks and the PR drops on LW crests where wave breaking intensifies (in line with Figs. 4 and 5, scatter plots). At large incidence angles and in the upwind direction, forward faces of active breakers are exposed. Hence, NRCS peaks are formed by the fast scatters that lead to strong asymmetry of Doppler spectra and the deviation between DV-derived and wave gauge elevation spectra [see Figs. 5(l) and 7(d)]. In contrast, at moderate incidence angles, NRCS spikes correspond to the slow facets (embedded in the water), which lead neither to the significant asymmetry of Doppler spectra [see Fig. 5(f) and (i)] nor the apparent deviation between DV-derived and wave gauge spectra [see Fig. 7(b) and (c)]. Note also that this paradigm and the data do not support the Hansen *et al.* [34] assumption that the DV of an "individual" breaker corresponds to the phase velocity of carrying wave at any incidence angle.

V. RADAR MTF

Wave-induced DV variations are used to assess the radar MTF (5). To take into account possible deviations of DV from LW orbital velocities, the DV response function μ defined by (6) is included in the radar MTF estimate (5) as

$$M = \mu^{1/2} \frac{gGS_{\sigma v}}{\overline{\sigma} \omega S_{vv}}. \tag{9}$$

Examples of estimated MTF's are shown in Fig. 7. Swell cases [e.g., cases like Fig. 7(d)], as well as cases with low coherence (<0.2) were excluded from our analysis. Spectral dependence of MTF in the frequency range of resolved wind waves from $f_p \approx 0.2$ Hz to $f_{\text{cut}} = 0.3$–0.8 Hz (that depends on the look geometry; see Appendix A for details) is not accounted for. Instead, the mean MTF averaged over $f_p < f < f_{\text{cut}}$ is used for each data sample. The mean MTF

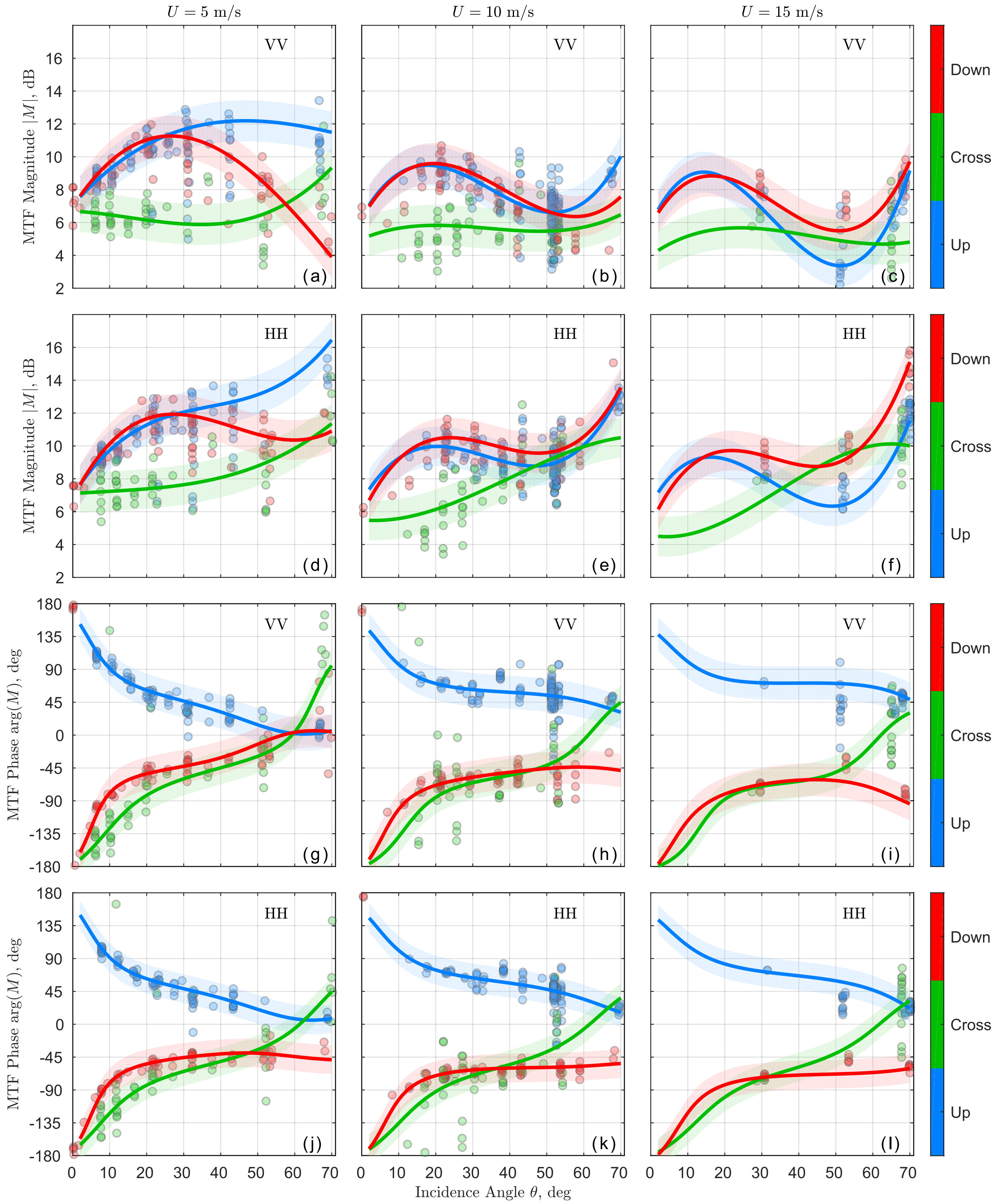

Fig. 9. Measured (circles) and fit (lines) MTF averaged over resolved wave frequencies, $f_p < f < f_{\text{cut}}$. Measurements are binned in wind speed ($U \pm 2.5$ m/s) and azimuth ($\phi \pm 45°$). Confidence intervals (shading) correspond to RMSE of the MTF fit (see Appendix C for details). (a)–(c) VV magnitude. (d)–(f) HH magnitude. (g)–(i) VV phase. (j)–(l) HH phase. (Left) $U = 5$ m/s. (Middle) $U = 10$ m/s.

is fit by empirical polynomials of incidence angle, azimuth, and wind speed (see Appendix C for details).

MTF magnitude [see Fig. 9(a)–(f)] has a local maximum around $\theta = 20°$ and a local minimum around $\theta = 50°$. A plausible explanation is related to the tilt-MTF, which has a maximum around $\theta = 20°$ (where radar scattering switches from the specular to the resonant mechanism) (see Fig. 11). Due to modulation of surface density of breakers by LW,

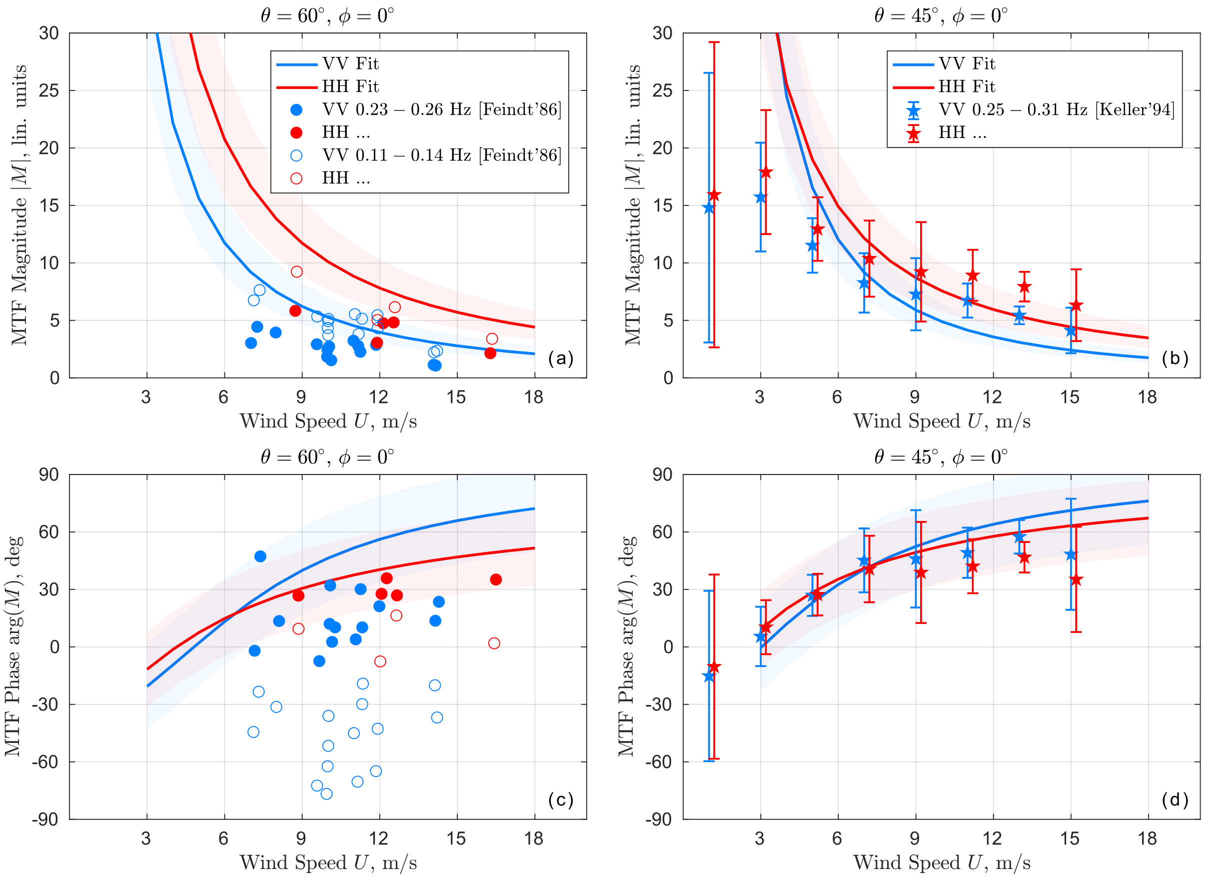

Fig. 10. Upwind MTF fit versus wind speed in comparison with data of (a) and (c) Feindt *et al.* [6] (at $\theta = 60°$) and (b) and (d) Keller *et al.* [7] (at $\theta = 45°$). Confidence intervals are the same as in Fig. 9. (a) and (b) MTF magnitude. (c) and (d) MTF phase.

the MTF magnitude increases at $\theta > 50°$ (with a stronger impact on HH), which may explain the local MTF minimum around 50°. This is not the case for light winds and VV polarization [see Fig. 9(a)] for which Bragg backscattering dominates over breaking backscattering.

As expected from the previous studies [6], [16], VV MTF magnitude is generally smaller than HH MTF magnitude that is likely attributed to stronger tilt modulation at HH polarization. At $20° < \theta < 50°$, the MTF phase is approximately independent of incidence angle with NRCS modulation maxima locating on the front/rear LW slope for the upwind/downwind radar azimuth, respectively.

Crosswind MTF phase switches sharply from positive to negative angles at $\theta = 60°$. Noting that tilt-MTF zeros in the crosswind direction and disregarding possible errors in radar-to-wind/wave azimuth, such a behavior indicates that backscattering peak moves from rear wave slopes at $\theta < 60°$ to front wave slopes at $\theta > 60°$.

To the best of our knowledge, there are two publications on the analysis of Ka-band MTF; they are both based on measurements taken from the NORDSEE platform located in 30-m deep water, similar to the Black Sea platform. Feindt *et al.* [6] reported the Ka-band measurements from 30.5 m height at $\theta = 60°$, mostly upwind azimuths, and presented radar MTF values averaged over two frequency ranges ($0.11 < f < 0.14$ Hz corresponding to swell and $0.23 < f < 0.26$ Hz corresponding to wind sea). Keller *et al.* [7] data were collected at $\theta = 45°$ at different radar heights and radar-wind azimuths (in the upwind to crosswind sector). The reported MTF represents the mean values averaged over wind wave frequencies ($0.25 < f < 0.3125$ Hz).

Wind dependence of our MTF magnitude [see Fig. 10(a) and (b)] is in good agreement with Keller *et al.* [7] for VV polarization except at $U < 4$ m/s. For HH polarization, our MTF is higher at $U < 9$ m/s. Feindt *et al.* [6] data averaged over the wind wave frequency range (similar to our resolved frequency range) are almost two times lower for both polarizations. Feindt *et al.* [6] data averaged over the swell frequency range agree better with our estimations obtained, however, for higher frequencies.

The MTF phase [see Fig. 10(c) and (d)] from our observations agrees well with Keller *et al.* [7] measurements, but is shifted toward wave crests in comparison with Feindt *et al.* [6]. One of the key points of Feindt *et al.* [6] is the negative VV MTF phase at low frequencies [swell, shown by empty circles in Fig. 10(c)]. This observation differs from either Keller *et al.* [7] or our data. Note also that Keller *et al.* [7] observed negative MTF phases at $\phi = 67.5°$ (see a middle row in their Fig. 4). This agrees with our azimuthal dependence of the MTF phase discussed in Fig. 9.

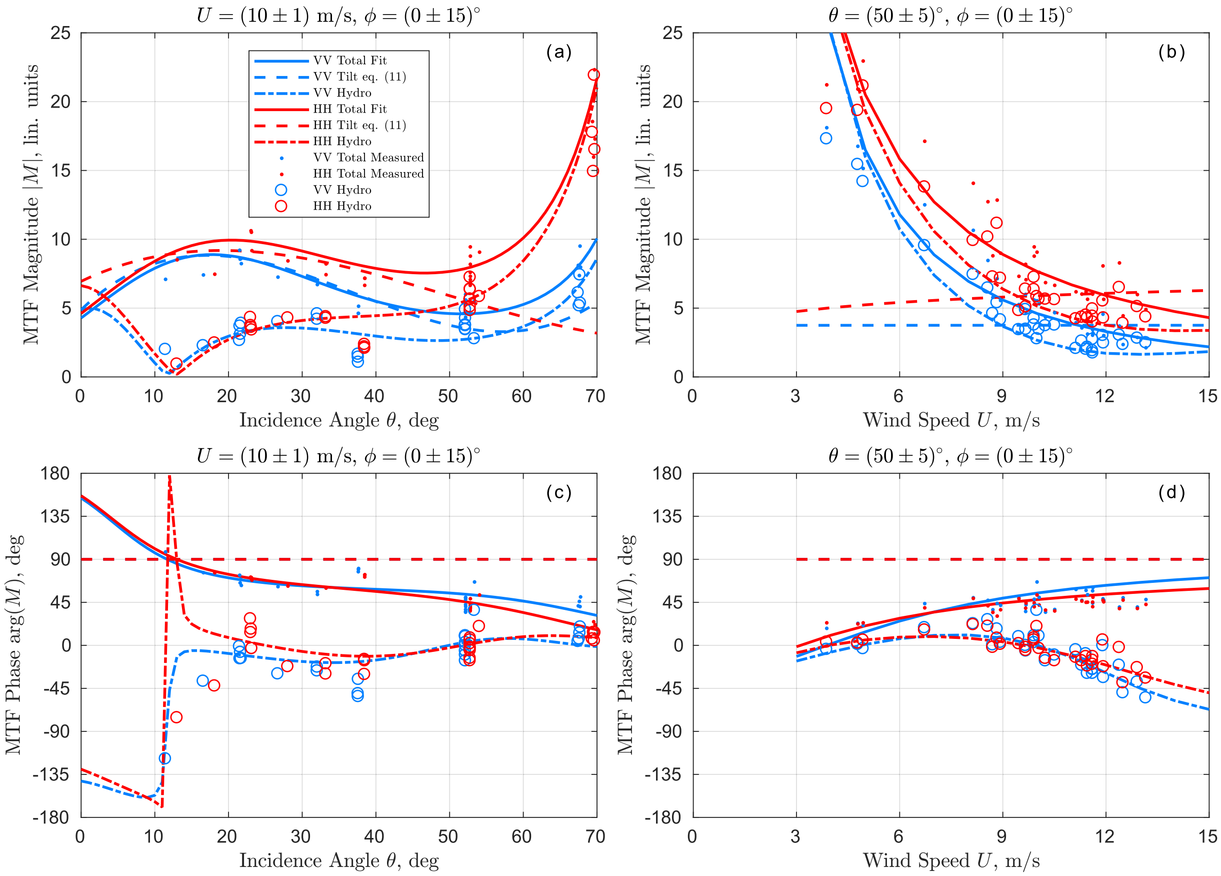

Fig. 11. (a) and (b) Magnitude and (c) and (d) phase of total (solid lines—fit and dots—data), tilt (dashed lines—theory), and hydrodynamics (dashed dotted lines—fit and circles—data) MTF for VV (blue line) and HH (red line) polarization versus (a) and (c) incidence angle and (b) and (d) wind speed.

Although some discrepancies at light winds, possibly resulted from different radar signal-to-noise ratios, our MTF fit generally agrees with Keller *et al.* [7]. Next, the role of tilt and hydrodynamics MTF components is analyzed in more detail.

A. Tilt and Hydrodynamics MTF

The total MTF can be partitioned into the tilt and hydrodynamics (hydro) components

$$M^{\mathrm{pp}} = M_T^{\mathrm{pp}} + M_H^{\mathrm{pp}}. \tag{10}$$

The tilt-MTF, M_T^{pp}, describes NRCS modulation caused by the LW-induced change of the local incidence angle. To the first order, it can be estimated from the incidence angle dependence of NRCS

$$M_T^{\mathrm{pp}} = \frac{1}{\overline{\sigma^{\mathrm{pp}}}} \frac{\partial \sigma^{\mathrm{pp}}}{\partial \theta} \cos \phi. \tag{11}$$

The tilt-MTF calculated from observed $\overline{\sigma^{\mathrm{pp}}}$ (we used geophysical model function KaDPMod suggested in [18]) is shown in Fig. 11. Its noticeable feature is an inverse behavior at large incidence angles, $M_T^{\mathrm{hh}} > M_T^{\mathrm{vv}}$, that differs from the "expected" Bragg theory behavior. However, this is not surprising, because NP backscattering from breaking waves significantly contributes to the NRCS, especially at HH, resulting in flattening of $\sigma^{\mathrm{hh}}(\theta)$ at large incidence angles (see [16, Sec. 2.2, Fig. 2] for more discussion). As discussed in [18], this effect is accounted for by the KaDPMod.

The hydro-MTF, M_H^{pp}, which describes NRCS modulation due to LW-induced modulation of short-scale scatterers, is then obtained by subtracting M_T from the total MTF

$$M_H^{\mathrm{pp}} = M^{\mathrm{pp}} - M_T^{\mathrm{pp}}. \tag{12}$$

Observed total, tilt-, and hydro-MTF (both direct measurements and fits) versus incidence angles and wind speed are shown in Fig. 11. The most striking feature of hydro-MTF is its dependence on polarization that certainly contradicts the pure Bragg scattering paradigm. The magnitude of hydro-MTF is systematically higher at HH polarization (see Fig. 11). This is in line with the PR (see Fig. 5), which is systematically lower than TSM PR. Lower PR indicates an important role of the NP associated with radar returns from breaking waves (at moderate incidence angles) and specular reflections from "large-scale" slopes of regular waves (at low incidence angles). The relative impact of the NP is defined by its partial contribution to the total NRCS, $p^{\mathrm{pp}} = \sigma_{\mathrm{np}}/\sigma^{\mathrm{pp}}$. Since $p^{\mathrm{hh}} > p^{\mathrm{vv}}$ (see [18] for more details), the modulation of scattering facets providing NP backscattering has different relative impacts on the hydrodynamics modulation at VV and HH, and thus results in the polarization dependence of the hydro-MTF. Modulation of short-scale wave breaking by LW is rather strong with MTF magnitudes as large as ≈ 20 [32], [35]. Such strong wave breaking modulation explains the observed difference

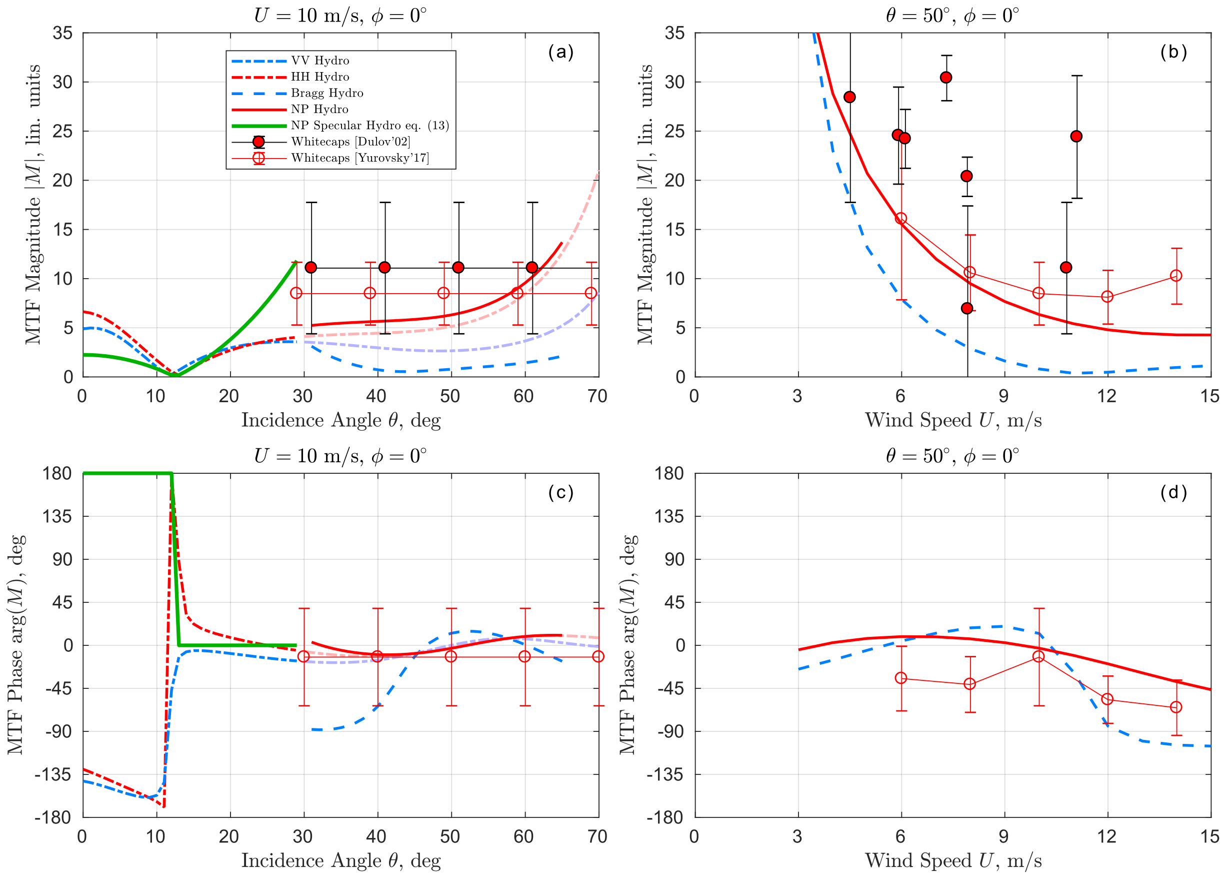

Fig. 12. Same as Fig. 11 for hydro-MTF (dashed dotted lines), Bragg spectral MTF (blue dashed lines), and NP MTF (red solid lines). Green lines are the theoretical hydro-MTF (13). Empirical estimates of whitecap MTF from [32] (closed circles) and [38] (open circles). (a) and (b) Magnitude and (c) and (d) phase of hydro-MTF (dashed dotted lines), Bragg spectral MTF (blue dashed lines), and NP MTF (red solid lines).

between HH and VV hydro-MTF and its increase at large θ [see Fig. 11(a)].

Another interesting feature of the observed hydro-MTF is its behavior at low incidence angles $\theta < 20°$ [see Fig. 11(a) and (c)]. First, there is almost no difference between VV and HH hydro-MTF at these θ values. This is in line with the dominant NP contribution to the total NRCS at near-nadir θ. Second, the amplitude of hydro-MTF almost zeros and its phase jumps from 0° to 180° at around $\theta = 13°$. This sharp behavior is consistent with so-called "contrast inversion" concept adopted in the sun glitter theory [36], [37]. According to this concept, the hydro-MTF is defined by the variations of the mean square slope (MSS)

$$M_H = (\tan^2\theta/\zeta^2 - 1)M_\zeta \tag{13}$$

where ζ^2 is the large-scale surface wave MSS (in terms of the composite scattering model), and $M_\zeta = 9/4$ is the MSS MTF (see [36, eqs. (12) and (14)]). With $\zeta^2 = 0.053$, this equation describes the observed vanishing of M_H^{pp} at $\theta = 13°$.

Observed decrease of M_H^{pp} amplitude with increasing wind speed [see Fig. 11(b)] is in line with the relaxation theory and associated decrease of the relaxation time (inversely proportional to wind speed squared). But, M_H^{pp} phase shift from LW crests (at moderate winds) toward backward LW slopes (at higher winds) conflicts the relaxation theory. A possible reason for such discrepancy may be related to wind aerodynamic effects leading to short wave enhancement on the rear (windward) LW slope, where the airflow is accelerated. Such a shift may also be related to the location and spread of enhanced scattering area during breaking events that lags behind wave crests and thus shifts onto rear slopes of LWs.

B. Partitioning of Hydro-MTF

Following [19], the NRCS is decomposed as a sum of two components, $\sigma^{\mathrm{pp}} = \sigma_{\mathrm{br}}^{\mathrm{pp}} + \sigma_{\mathrm{np}}$, supported by Bragg scattering, $\sigma_{\mathrm{br}}^{\mathrm{pp}}$, and NP scattering, σ_{np}. The latter component is related to specular reflection from breaking events at moderate and large θ and from slopes of regular (nonbreaking) waves at low to nadir θ. Synchronous copolarized measurements enable to separate the two components and investigate them separately [19]. Similarly, the hydro-MTF can also be decomposed into NRCS modulations supported by Bragg and non-Bragg scattering mechanisms

$$M_H^{\mathrm{pp}} = (1 - p^{\mathrm{pp}})M_{\mathrm{br}}^{\mathrm{pp}} + p^{\mathrm{pp}} M_{\mathrm{np}} \tag{14}$$

where $p^{\mathrm{pp}} = \sigma_{\mathrm{np}}/\sigma^{\mathrm{pp}}$ is the relative NP contribution to the total NRCS, which can be assessed from copolarized NRCS measurements and theoretical PR for Bragg scattering [18]. Hydro-MTF for Bragg scattering in (14) consists of two terms associated with the pure Bragg wave spectrum MTF and an additional contribution from modulation of the MSS of large-scale surface waves (in terms of the two-scale Bragg model, see [16, eq. (19)] for more details)

$$M_{\text{br}}^{\text{pp}} = M_{0\text{br}} + \frac{g^{\text{pp}}\zeta^2}{1+g^{\text{pp}}\zeta^2} M_\zeta \tag{15}$$

where g^{pp} is the geometrical coefficient (see Appendix B for details). As explained in [16], the effect of MSS modulation on the Bragg MTF is weak and can be ignored. Thus, hereinafter, $M_{\text{br}}^{\text{pp}}$ in (15) is solely associated with the pure Bragg MTF, $M_{0\text{br}}$, which is independent of polarization.

Similar to the NRCS decomposition [19], the hydro-MTF at VV and HH polarizations, M_H^{vv} and M_H^{hh}, allows to separate the pure Bragg spectral MTF, $M_{0\text{br}}$, and MTF for NP scattering, M_{np}

$$M_{0\text{br}} = \frac{M_H^{\text{vv}} p^{\text{hh}} - M_H^{\text{hh}} p^{\text{vv}}}{p^{\text{hh}} - p^{\text{vv}}} \tag{16}$$

$$M_{\text{np}} = \frac{M_H^{\text{hh}}(1-p^{\text{vv}}) - M_H^{\text{vv}}(1-p^{\text{hh}})}{p^{\text{hh}} - p^{\text{vv}}}. \tag{17}$$

Estimates of Bragg and NP components of hydro-MTF are accompanied in Fig. 12 by independent measurements of whitecap MTF [32], [38] performed from the same site, but using different optical sensors and techniques. The estimates of MTF components are not shown for $\theta < 30°$, where specular reflections dominate and partial contributions for VV and HH are close. As an alternative, the hydro-MTF based on the specular reflection model (13) is shown in Fig. 12(a) and (c) for low incidence angles $\theta < 30°$, which extends the incidence angle dependence of NP MTF over the entire range of observed θ. This model underestimates MTF magnitude at near nadir angles in comparison with observed values if theoretical MSS MTF is used, $M_s = 9/4$ [36].

Fig. 12(a) and (c) suggests that wave breaking MTF and specular reflection MTF (linked to the MSS) are quite consistent and exhibit "smooth" transition between NP modulation by breaking waves (moderate incidence, $\theta > 30°$) and NP modulation by specular reflection from nonbreaking waves (at low incidence angles $\theta < 30°$). At $\theta > 13°$, the phase of both NP MTFs is close to zero suggesting that either wave breaking or a number of specular points (related to the MSS) is enhanced on the crests of modulating LW. At small incidence angles $\theta < 13°$, enhanced MSS results in decreased specular reflectivity, and thus, the MTF phase "suddenly" jumps by 180° toward smoother wave troughs.

The magnitude of wave breaking MTF and the magnitude of spectral MTF at the Bragg wavenumber both decrease with wind speed [see Fig. 12(b)]. This is explained by the corresponding decrease of the wave relaxation time that becomes much smaller than the period of modulating LW. Wave breaking modulations (inferred from Ka-band radar data) are consistent with whitecap modulations quasi-synchronously measured within the radar footprint [38], though some discrepancies are noticeable at the highest observed wind. Experimental estimates of whitecap coverage from joint optical and wave gauge measurements [32] demonstrate even larger MTF amplitudes. The phase of radar wave breaking MTF indicates an enhancement of breakers over the LW crests. Some tendency indicating a shift toward the rear slope of LW at high winds is also apparent. This tendency is consistent with the observed phase of whitecap MTF [see Fig. 12(d)].

The following qualitative interpretation may be given to explain the observed shift of M_{np} phase toward rear slopes of the LW. First, it is assumed that wave breaking contributes to the NRCS and is strongly modulated by the LW. Wave breaking crest instability develops over LW crests following short-wave and LW-current interaction. This local area of enhanced instability propagates with LW phase velocity. Yet, once an unstable crest breaks, it generates disturbances and foam embedded in the water in the LW crest area and thus starts moving with the LW orbital velocity. As the LW crest keeps moving forward with its phase speed, these disturbances inevitably shift down the LW rear slope toward its following trough. The resulting enhanced roughness patch responsible for radar backscattering becomes distributed between the LW crest (initial starting point of the instabilities) and the following trough, as observed in Fig. 12(d). Note, this interpretation is consistent with unexpectedly low DV corresponding to breaking events (see Figs. 4 and 5).

Finally, Ka-band Bragg waves (wavelengths from 5 to 10 mm) are strongly modulated by LW at low winds [see Fig. 11(b)]. Such short ripples are primarily generated as the parasitic, bound capillaries due to the microscale breaking of short gravity wave crests, and thus have the phase velocity equal to the phase velocity of the breaking gravity wave [39], [40]. Energy pumping to parasitic capillaries is proportional to the dissipation of short gravity waves (see [16], [40], [41] for more details and references). Modulation of short gravity waves by LW results in modulation of microscale breaking and corresponding modulation of parasitic capillaries. Due to the cascade mechanism of capillary wave modulation, the MTF of parasitic capillaries corresponds to the MTF of microscale wave breaking. That is what seems to be revealed in Fig. 11(b) at low winds, where the Bragg wave MTF is comparable in magnitude to the NP MTF. At moderate-to-high winds, the "direct generation" of capillary waves by the wind becomes the dominant energy source. Because the relaxation time of capillary waves is much smaller than the period of modulating LW, their modulations tend to disappear at high winds [see Fig. 11(b)]. Note that small amplitude of MTF can lead to unstable estimates of its phase. Therefore, the MTF phase corresponding to MTF amplitude less than ≈ 2 can be disregarded. Interestingly, the phase of the Bragg MTF is negative at $U > 10$ m/s (the maximum of roughness is on the rear, windward wave slope). This negative phase agrees with Feindt *et al.* [6] who have attributed it to the effect of air flow modulation over the LW. But, as mentioned earlier, the Bragg MTF phase at $U > 10$ m/s is subject to errors due to the weak Bragg MTF magnitude.

VI. CONCLUSION

This paper continues the analysis of dual copolarized (VV and HH) Ka-band radar backscatter measurements from the sea surface taken from the Black Sea Research platform. While the previous analysis has targeted the time mean properties of Ka-band NRCS [18], this paper focuses on the modulation properties of the NRCS and DV on space-time scales corresponding to "long" surface waves (LW) in a frequency range from 0.2 to 0.8 Hz.

LW-induced variations of the Doppler radar signal, NRCS, and DV, derived from quasi-instantaneous Doppler spectra (averaged over 0.2-s time intervals), reveal the following remarkable features. First, NRCS and DV modulations are well correlated. Unlike the DV (that is visually quite smooth), the NRCS signal exhibits a spiky structure, i.e., large transient enhancements of the NRCS with peaks much larger than the overall background. As expected, HH NRCS modulations are stronger than VV ones that lead to modulations of the PR, PR = VV/HH. This suggests that the important source of the NRCS modulation is the modulation of scattering facets providing NP radar return. These facets likely correspond to wave breaking events at moderate and large θ or to specular surface slopes at low to nadir θ.

The statistical distribution of LW-induced variations of the NRCS and DV are different. The pdf of the NRCS (in linear units) is strongly skewed in a wide range of incidence angles that confirm the presence of spikelike events associated with wave breaking. In contrast, the skewness of DV pdf is much smaller at moderate and low incidence angles. This suggests that the DV of NRCS spikes is "low," i.e., it is not locked to the phase velocity of breaking waves. As a consequence, LW elevation spectra derived from DV measurements are very close to LW elevation spectra measured by the wave gauge. Unlike, at large incidence angles ($\theta = 70°$) and HH polarization, the DV pdf is strongly skewed and DV-derived LW elevation spectra deviate significantly from wave gauge elevation spectra. This indicates that breakers are detected by a radar as "fast scatterers" at large incidence angles.

In order to reconcile DV measurements at moderate and large incidence angles, the following paradigm is suggested. First, it is assumed that a breaker advances with the phase velocity and leaves behind an expanding area of enhanced surface roughness "embedded in the water." Forward faces of active breakers are exposed at large incidence angles and in the upwind direction. At these observation conditions, NRCS peaks are formed by the fast scatters that lead to strong asymmetry of Doppler spectra and deviation between DV-derived and wave gauge elevation spectra. In contrast, at moderate incidence angles, NRCS spikes correspond to the slow facets (embedded into the water) on the tops of breakers, which leads neither to significant asymmetry of Doppler spectra nor apparent deviation between DV-derived and wave gauge spectra.

After splitting the MTF into tilt component and hydrocomponent, the hydro-MTF is found to be polarization dependent with higher HH amplitudes. This certainly contradicts the standard Bragg scattering theory and points to the nonnegligible contribution of NP scattering from wave breaking. Depending on wind speed, the NP modulations are significant with MTF amplitude varying from 5 to about 30. At low-to-moderate winds, breakers locate on the crests of modulating LW. Above 10 m/s, the maximum of breaker modulation shifts toward the rear LW slopes.

At low incidence angles ($\theta < 30°$), NP scattering is dominated by specular reflections from slopes of regular (nonbreaking) waves. The observed hydro-MTF at such θ exhibits features anticipated from the quasi-specular reflection theory. In particular, its amplitude zeros in the vicinity of the incidence angle corresponding to MSS of the large-scale surface waves. This is accompanied by an abrupt change of the MTF phase by 180°. Combination of observed wave breaking MTF ($\theta > 30°$) and theoretical specular point MTF ($\theta < 30°$) provides a proxy for a consistent description of the NP hydro-MTF in the full range of observed incidence angles.

The spectral MTF of the resonant Bragg scattering is essential only at low winds where its magnitude is comparable to the magnitude of the wave breaking MTF. Because Ka-band Bragg waves are parasitic capillaries at low winds, their modulations are related to the modulations of microscale breaking of short gravity waves. At winds above 8 m/s, the direct generation by wind becomes increasingly important for Ka-band Bragg millimeter scale waves, and thus, their modulation is significantly suppressed by wind forcing and weakly contributes to the hydro-MTF.

These observations provide deeper insights into the physics of surface wave modulations and millimeter wavelength radar backscattering from the ocean surface. This is needed for the development of new space-borne Ka-band instruments and better retrieval of the sea surface characteristics via a synergy of microwave and optical remote sensing techniques (see [42], [43]). The proposed parameterization of the Ka-band radar MTF can further be used to assess the wave-induced contribution to the mean DV. This is essential for better separation of Doppler shift components due to ocean currents and wave-induced motions.

APPENDIX A
CORRECTION FOR THE RADAR PATTERN

Spatial filtering by an RP footprint is represented as the wavenumber filter response function [44]

$$\gamma(\mathbf{k}) = \frac{|\mathrm{FFT2}(\gamma(\mathbf{x}))|^2}{\langle \gamma(\mathbf{x}) \rangle} \tag{18}$$

where $\mathbf{k}$ is the wavenumber vector, $\langle \ldots \rangle$ denotes spatial averaging, and $\gamma(\mathbf{x})$ is the two-way RP projected on the sea surface plane and accounting for the R^{-4} distance fading and the incidence angle dependence of NRCS

$$\gamma(\mathbf{x}) = \frac{\Gamma(\mathbf{x}) R(\mathbf{x})^{-4} \sigma(\mathbf{x})}{R(\mathbf{x}_0)^{-4} \sigma(\mathbf{x}_0)} \tag{19}$$

where $\mathbf{x}$ is the local point on the sea surface, $\mathbf{x}_0$ is the intersection point of the radar axis and sea surface, R is the distance from the radar to the local point on the sea surface, σ is the NRCS at the local point (evaluated from NRCS model [18]), Γ is the two-way RP known from calibration (see [18, Appendix] for details) and projected on the sea surface. Examples of RP projection $\gamma(\mathbf{x})$ and its wavenumber response function $\gamma(\mathbf{k})$ are given in Fig. 13.

Wavenumber response function $\gamma(\mathbf{k})$ is then projected onto frequency-azimuth space using the deep water dispersion relationship, $(2\pi f)^2 = gk$, yielding frequency-azimuth response

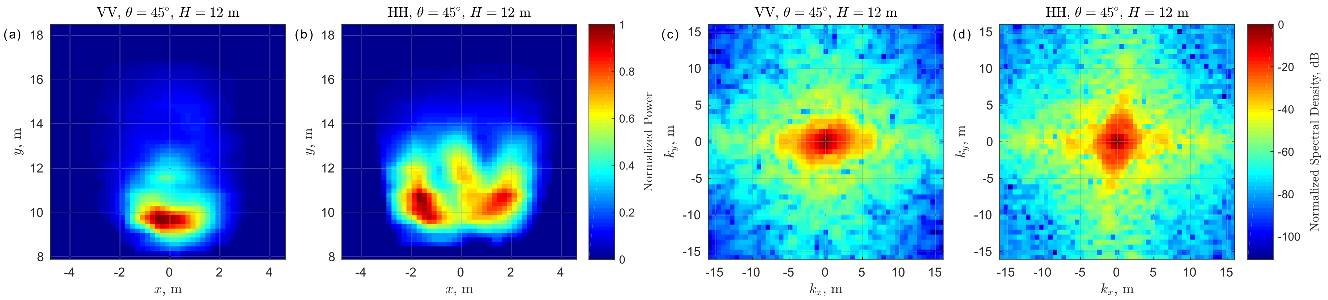

Fig. 13. (a) and (b) Example of RP projection on the sea surface and (c) and (d) its response in the wavenumber space for (a) and (c) VV and (b) and (d) HH polarizations. Incidence angle is 45°, upwind azimuth, 10 m/s wind speed, and radar height is 12 m.

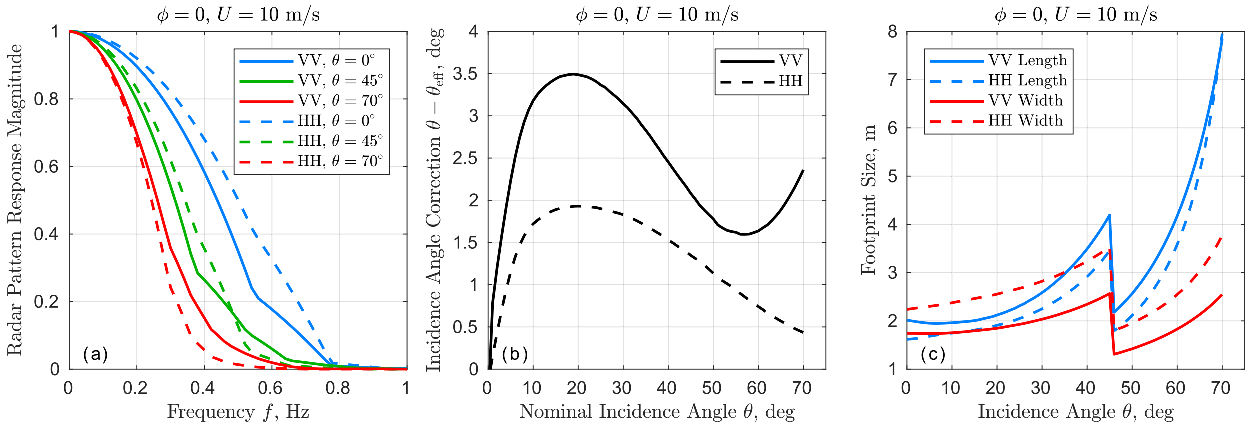

Fig. 14. (a) RP response versus wave frequency, (b) incidence angle correction $\theta - \theta_{\text{eff}}$ versus nominal incidence angle θ, and (c) −3 dB ground radar footprint size (cross-look width and in-look length) versus incidence angle (the jump at $\theta = 45°$ corresponds to the change in radar height from 12 to 6 m).

function $\gamma\,(f, \phi)$ that is used for the correction of radar spectra at given θ, ϕ, U

$$S'_{pq}(f) = S_{pq}(f)\gamma\,(f)^{-1} \tag{20}$$

where p and q are either DV, v, or NRCS, σ.

The above correction is important only for the radar-derived elevation spectra $S_{\xi\xi}$ [see (8)] and the DV response function μ [see (6)]. For the traditional MTF, M [see (4)], the corrections included in the nominator and denominator cancel each other.

A specific antenna design results in different VV and HH response functions [see Fig. 13(c) and (d)]. In particular, HH channel passes higher/lower frequencies than VV channel in the radar-look/cross-look direction, respectively. The cutoff frequency of an RP frequency response function [see Fig. 14(a)] decreases from 0.5 Hz at near-nadir θ to 0.25 Hz at $\theta = 70°$. This study analysis is limited to frequencies lower than the cutoff frequency, f_{cut} corresponding to 0.25 of the maximum RP response magnitude. At $f < f_{\text{cut}}$, the correction (20) effectively accounts for the effect of RP spatial filtering.

Finite RP angular width along with strong incidence angle dependence of the sea surface NRCS, result in shifting of the footprint centroid, $\mathbf{x}_{\text{eff}} = \int \mathbf{x}\gamma\,(\mathbf{x})d\mathbf{x})/\int \gamma\,(\mathbf{x})d\mathbf{x}$, and corresponding decrease of the effective incidence angle, $\theta_{\text{eff}} = \arctan(|\mathbf{x}_{\text{eff}}|/H)$, where H is the radar height. Deviation of the nominal incidence angle (corresponding to geometrical radar axis) from the effective one, $\theta - \theta_{\text{eff}}$, is always positive and peaks at $\theta \approx 20°$, where $\sigma\,(\theta)$ has the largest gradient [see Fig. 14(b)]. At high incidence angles, the deviation increases because of rapid distance fading, R^{-4}. This deviation is stronger for VV polarization, because the angular width of VV RP is larger than that of HH RP in the range direction. Typical deviation from the nominal θ is below 3.5° and 2° for VV and HH polarization, respectively, at $U = 10$ m/s. The above correction is applied to all analyzed data.

A ground size of the RP footprint in the range (length) and the cross-look (width) directions translates into the corresponding RP frequency response [see Fig. 14(c)]. The jump in RP footprint size is caused by change in radar height at $\theta = 45°$.

APPENDIX B
TWO-SCALE MODEL EVALUATION

The Bragg theory prediction of the PR is based on the classical two-scale model (TSM, [45], [46]) that involves a separation of wave scales onto short resonant Bragg waves with wavenumber, $k_{\text{br}} = 2k_r \sin\theta$, and longer modulating waves, $k < k_{\text{br}}/4$. TSM PR estimate follows [41] and is based on the following set of equations:

$$\text{PR}_{\text{br}} = \frac{|G_{\text{vv}}|^2\left(1 + g_{\text{vv}}\zeta_i^2\right)}{|G_{\text{hh}}|^2\left(1 + g_{\text{hh}}\zeta_i^2\right)} \tag{21}$$

$$g_{\text{vv}} = \frac{1}{2|G_{\text{vv}}|^2}\frac{\partial^2 |G_{\text{vv}}|^2}{\partial\theta^2} \tag{22}$$

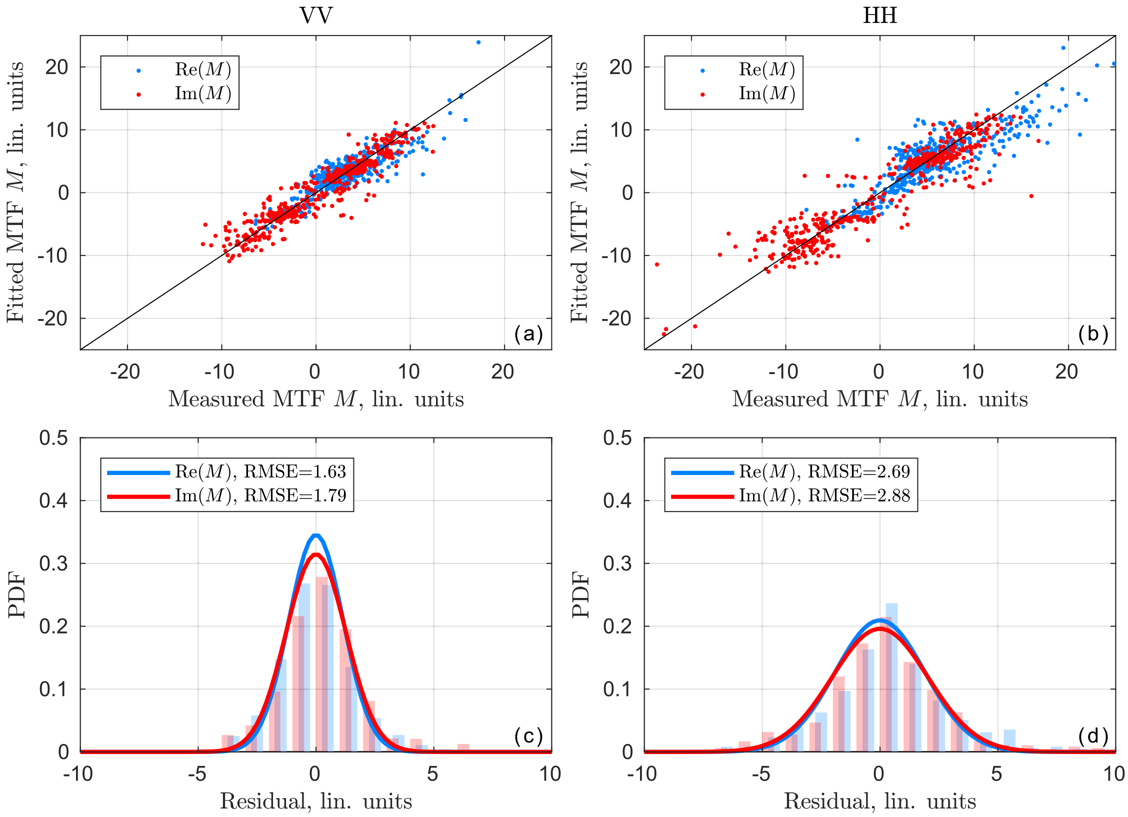

Fig. 15. (a) and (b) Scatter plots for fit versus measured MTF and (c) and (d) observed (bars) and gauss-fit (lines) residual distributions. (Left column) VV polarization [(a) and (c)]. (Right column) HH polarization [(b) and (d)]. Blue color is the real part of MTF. Red color is the imaginary part of MTF.

$$g_{\mathrm{hh}} = \frac{1}{2|G_{\mathrm{hh}}|^2}\frac{\partial^2|G_{\mathrm{hh}}|^2}{\partial\theta^2} + \frac{2}{\sin^2\theta}\frac{|G_{\mathrm{vv}}|}{|G_{\mathrm{hh}}|}\frac{\zeta_c^2}{\zeta_i^2} \tag{23}$$

$$G_{\mathrm{vv}} = \frac{[\epsilon + (\epsilon - 1)\sin^2\theta](\epsilon - 1)\cos^2\theta}{[\epsilon\cos\theta + (\epsilon - \sin^2\theta)^{1/2}]^2} \tag{24}$$

$$G_{\mathrm{hh}} = \frac{(\epsilon - 1)\cos^2\theta}{[\cos\theta + (\epsilon - \sin^2\theta)^{1/2}]^2} \tag{25}$$

where $\epsilon = 17 - i28$ is the complex dielectric constant of sea water in the Ka-band for 20° temperature and 18-g/kg salinity [47], and ζ_i^2 and ζ_c^2 is the MSS of modulating waves in the incidence plane and in the plane normal to the incidence plane, respectively.

APPENDIX C
FITTING OF THE MTF

An MTF fitting function is based on empirical polynomials of incidence angle θ, azimuth ϕ, and wind speed U. The fitting improves if magnitude and phase are fit independently. To account for the wide range of MTF magnitude, it is fit in logarithmic units (dB). Magnitude $\log(|M|)$ and phase $M/|M|$ are fit as

$$\begin{bmatrix}\log(|M|)\\ M/|M|\end{bmatrix} = \sum_{i=0}^{n}\sum_{j=0}^{2}\sum_{k=0}^{1}\begin{bmatrix}B_{ijk}\\ C_{ijk}\end{bmatrix}\theta^i\cos(j\phi)(\log U)^k \tag{26}$$

where $n = 3$ is the polynomial degree selected empirically. Resulting fit represents MTF magnitude in dB units (see Fig. 9). For further analysis, it is converted back to linear units (see Fig. 11).

TABLE I
RMSEs AND CHI-SQUARE TESTS OF MTF FIT

Parameter	VV RMSE	HH RMSE	VV χ^2	HH χ^2
$\|M\|$, dB	1.25	1.21	3.48	3.06
$\|M\|$, lin. units	1.69	2.81	11.81	10.81
arg(M), deg	22.69	19.69	0.62	1.49
Re(M), lin. units	1.63	2.69	5.14	5.78
Im(M), lin. units	1.79	2.88	8.98	6.38

Critical χ^2 for 5% significance level and 7 degrees of freedom is 14.07.

The distribution of fitting residuals (Fig. 15) is quasi-Gaussian as suggested by χ^2-tests (see Table I). But, a root-mean-square error (RMSE) of HH fit is larger than that of VV fit. This may be a consequence of unresolved variability present in the HH signal. In particular, wave breaking leads to more spiky HH backscattering, which is less suitable for the linear MTF analysis. An RMSE for MTF magnitude and phase as well as for real and imaginary MTF components (see Table I) is used to plot confidence intervals in Fig. 9. Coefficients B_{ijk} and C_{ijk} from (26) are given in Table II.

ACKNOWLEDGMENT

The authors would like to thank E. Rodriguez, B. Plant, W. Alpers, and anonymous referees who made very helpful

TABLE II

COEFFICIENTS B_{ijk} AND C_{ijk}

Index			VV polarization			HH polarization		
i	j	k	B_{ijk}	$\mathrm{Re}(C_{ijk})$	$\mathrm{Im}(C_{ijk})$	B_{ijk}	$\mathrm{Re}(C_{ijk})$	$\mathrm{Im}(C_{ijk})$
0	0	0	$+2.224 \cdot 10^{0}$	$-1.184 \cdot 10^{0}$	$-2.027 \cdot 10^{-1}$	$+2.214 \cdot 10^{0}$	$-1.122 \cdot 10^{0}$	$-2.347 \cdot 10^{-1}$
1	0	0	$-2.069 \cdot 10^{-2}$	$+1.339 \cdot 10^{-1}$	$-4.231 \cdot 10^{-2}$	$+4.959 \cdot 10^{-2}$	$+1.588 \cdot 10^{-1}$	$-4.202 \cdot 10^{-2}$
2	0	0	$+1.972 \cdot 10^{-3}$	$-1.967 \cdot 10^{-3}$	$+1.006 \cdot 10^{-3}$	$-1.057 \cdot 10^{-3}$	$-3.469 \cdot 10^{-3}$	$+1.198 \cdot 10^{-3}$
3	0	0	$-2.336 \cdot 10^{-5}$	$+6.323 \cdot 10^{-6}$	$-3.506 \cdot 10^{-6}$	$+7.777 \cdot 10^{-6}$	$+2.335 \cdot 10^{-5}$	$-9.005 \cdot 10^{-6}$
0	1	0	$+2.880 \cdot 10^{-2}$	$-1.267 \cdot 10^{-1}$	$+1.135 \cdot 10^{-1}$	$-1.491 \cdot 10^{-1}$	$-1.542 \cdot 10^{-1}$	$+3.113 \cdot 10^{-1}$
1	1	0	$-4.146 \cdot 10^{-2}$	$-3.090 \cdot 10^{-2}$	$+1.416 \cdot 10^{-1}$	$-1.183 \cdot 10^{-2}$	$-1.595 \cdot 10^{-2}$	$+1.313 \cdot 10^{-1}$
2	1	0	$+2.106 \cdot 10^{-3}$	$+1.790 \cdot 10^{-3}$	$-5.720 \cdot 10^{-3}$	$+1.003 \cdot 10^{-3}$	$+1.088 \cdot 10^{-3}$	$-5.934 \cdot 10^{-3}$
3	1	0	$-1.515 \cdot 10^{-5}$	$-2.170 \cdot 10^{-5}$	$+4.877 \cdot 10^{-5}$	$-5.136 \cdot 10^{-6}$	$-1.345 \cdot 10^{-5}$	$+6.030 \cdot 10^{-5}$
0	2	0	$-2.262 \cdot 10^{-1}$	$-8.339 \cdot 10^{-2}$	$-4.235 \cdot 10^{-2}$	$-2.741 \cdot 10^{-1}$	$-7.071 \cdot 10^{-2}$	$+5.578 \cdot 10^{-2}$
1	2	0	$+3.944 \cdot 10^{-2}$	$+9.010 \cdot 10^{-2}$	$+8.950 \cdot 10^{-2}$	$+2.573 \cdot 10^{-2}$	$+6.652 \cdot 10^{-2}$	$+6.089 \cdot 10^{-2}$
2	2	0	$+1.220 \cdot 10^{-3}$	$-3.965 \cdot 10^{-3}$	$-2.931 \cdot 10^{-3}$	$+9.389 \cdot 10^{-4}$	$-2.622 \cdot 10^{-3}$	$-1.497 \cdot 10^{-3}$
3	2	0	$-2.845 \cdot 10^{-5}$	$+4.488 \cdot 10^{-5}$	$+2.351 \cdot 10^{-5}$	$-1.758 \cdot 10^{-5}$	$+2.668 \cdot 10^{-5}$	$+6.191 \cdot 10^{-6}$
0	0	1	$-4.021 \cdot 10^{-1}$	$+6.347 \cdot 10^{-2}$	$+1.426 \cdot 10^{-1}$	$-3.753 \cdot 10^{-1}$	$+5.339 \cdot 10^{-2}$	$+1.345 \cdot 10^{-1}$
1	0	1	$+3.357 \cdot 10^{-2}$	$-1.800 \cdot 10^{-2}$	$+3.808 \cdot 10^{-3}$	$-1.226 \cdot 10^{-3}$	$-3.355 \cdot 10^{-2}$	$+3.799 \cdot 10^{-3}$
2	0	1	$-1.741 \cdot 10^{-3}$	$+8.967 \cdot 10^{-5}$	$-1.564 \cdot 10^{-4}$	$-8.898 \cdot 10^{-5}$	$+8.825 \cdot 10^{-4}$	$-2.194 \cdot 10^{-4}$
3	0	1	$+1.835 \cdot 10^{-5}$	$+2.085 \cdot 10^{-6}$	$+6.570 \cdot 10^{-7}$	$+2.093 \cdot 10^{-6}$	$-6.237 \cdot 10^{-6}$	$+2.557 \cdot 10^{-6}$
0	1	1	$-9.136 \cdot 10^{-3}$	$+5.785 \cdot 10^{-2}$	$+3.167 \cdot 10^{-2}$	$+1.064 \cdot 10^{-1}$	$+8.523 \cdot 10^{-2}$	$-6.176 \cdot 10^{-2}$
1	1	1	$+1.886 \cdot 10^{-2}$	$+1.437 \cdot 10^{-2}$	$-3.362 \cdot 10^{-2}$	$+6.039 \cdot 10^{-4}$	$+3.372 \cdot 10^{-3}$	$-2.916 \cdot 10^{-2}$
2	1	1	$-1.015 \cdot 10^{-3}$	$-8.507 \cdot 10^{-4}$	$+1.778 \cdot 10^{-3}$	$-3.646 \cdot 10^{-4}$	$-3.287 \cdot 10^{-4}$	$+1.894 \cdot 10^{-3}$
3	1	1	$+8.185 \cdot 10^{-6}$	$+1.048 \cdot 10^{-5}$	$-1.632 \cdot 10^{-5}$	$+1.992 \cdot 10^{-6}$	$+4.641 \cdot 10^{-6}$	$-2.154 \cdot 10^{-5}$
0	2	1	$+1.626 \cdot 10^{-1}$	$+1.145 \cdot 10^{-1}$	$+6.235 \cdot 10^{-2}$	$+1.550 \cdot 10^{-1}$	$+8.275 \cdot 10^{-2}$	$+2.749 \cdot 10^{-2}$
1	2	1	$-2.149 \cdot 10^{-3}$	$-3.875 \cdot 10^{-2}$	$-3.247 \cdot 10^{-2}$	$+1.127 \cdot 10^{-2}$	$-2.423 \cdot 10^{-2}$	$-1.748 \cdot 10^{-2}$
2	2	1	$-1.076 \cdot 10^{-3}$	$+1.640 \cdot 10^{-3}$	$+1.260 \cdot 10^{-3}$	$-1.276 \cdot 10^{-3}$	$+8.987 \cdot 10^{-4}$	$+5.322 \cdot 10^{-4}$
3	2	1	$+1.725 \cdot 10^{-5}$	$-1.856 \cdot 10^{-5}$	$-1.184 \cdot 10^{-5}$	$+1.578 \cdot 10^{-5}$	$-9.139 \cdot 10^{-6}$	$-3.502 \cdot 10^{-6}$

comments and suggestions leading to improvements of this paper.

REFERENCES

[1] B. Chapron, F. Collard, and F. Ardhuin, "Direct measurements of ocean surface velocity from space: Interpretation and validation," *J. Geophys. Res. Oceans*, vol. 110, p. C07008, Jul. 2005, doi: 10.1029/2004JC002809.

[2] A. A. Mouche *et al.*, "On the use of Doppler shift for sea surface wind retrieval from SAR," *IEEE Trans. Geosci. Remote Sens.*, vol. 50, no. 7, pp. 2901–2909, Jul. 2012.

[3] A. C. H. Martin and C. Gommenginger, "Towards wide-swath high-resolution mapping of total ocean surface current vectors from space: Airborne proof-of-concept and validation," *Remote Sens. Environ.*, vol. 197, pp. 58–71, Aug. 2017.

[4] M. A. Bourassa, E. Rodriguez, and D. Chelton, "Winds and currents mission: Ability to observe mesoscale AIR/SEA coupling," in *Proc. Int. Geosci. Rem. Sens. Symp. (IGARSS)*, Beijing, China, Nov. 2016, pp. 7392–7395, doi: 10.1109/IGARSS.2016.7730928.

[5] F. Ardhuin *et al.*, "Measuring currents, ice drift, and waves from space: The sea surface kinematics multiscale monitoring (SKIM) concept," *Ocean Sci. Discuss.*, pp. 1–26, 2017, doi: 10.5194/os-2017-65.

[6] F. Feindt, J. Schröter, and W. Alpers, "Measurement of the ocean wave-radar modulation transfer function at 35 GHz from a sea-based platform in the North Sea," *J. Geophys. Res. Oceans*, vol. 91, no. C8, pp. 9701–9708, 1986.

[7] W. C. Keller, W. J. Plant, R. A. Petitt, Jr., and E. A. Terray, "Microwave backscatter from the sea: Modulation of received power and Doppler bandwidth by long waves," *J. Geophys. Res. Oceans*, vol. 99, no. C5, pp. 9751–9766, 1994.

[8] W. C. Keller and J. W. Wright, "Microwave scattering and the straining of wind-generated waves," *Radio Sci.*, vol. 10, no. 2, pp. 139–147, 1975.

[9] W. J. Plant, W. C. Keller, and A. Cross, "Parametric dependence of ocean wave-radar modulation transfer functions," *J. Geophys. Res. Oceans*, vol. 88, no. C14, pp. 9747–9756, 1983.

[10] J. Schröter, F. Feindt, W. Alpers, and W. C. Keller, "Measurement of the ocean wave-radar modulation transfer function at 4.3 GHz," *J. Geophys. Res. Oceans*, vol. 91, no. C1, pp. 923–932, 1986.

[11] D. E. Weissman and J. W. Johnson, "Measurements of ocean wave spectra and modulation transfer function with the airborne two-frequency scatterometer," *J. Geophys. Res. Oceans*, vol. 91, no. C2, pp. 2450–2460, 1986.

[12] T. Hara and W. J. Plant, "Hydrodynamic modulation of short wind-wave spectra by long waves and its measurement using microwave backscatter," *J. Geophys. Res. Oceans*, vol. 99, no. C5, pp. 9767–9784, 1994.

[13] S. A. Ermakov *et al.*, "On the Doppler frequency shifts of radar signals backscattered from the sea surface," *Radiophys. Quant. Electron.*, vol. 57, no. 4, pp. 239–250, 2014.

[14] W. Alpers and K. Hasselmann, "The two-frequency microwave technique for measuring ocean-wave spectra from an airplane or satellite," *Boundary-Layer Meteorol.*, vol. 13, nos. 1–4, pp. 215–230, 1978.

[15] R. Romeiser, A. Schmidt, and W. Alpers, "A three-scale composite surface model for the ocean wave–radar modulation transfer function," *J. Geophys. Res. Oceans*, vol. 99, no. C5, pp. 9785–9801, 1994.

[16] V. Kudryavtsev, D. Hauser, G. Caudal, and B. Chapron, "A semiempirical model of the normalized radar cross section of the sea surface, 2. Radar modulation transfer function," *J. Geophys. Res. Oceans*, vol. 108, pp. FET 3-1–FET 3-16, Mar. 2013, doi: 10.1029/2001JC001004.

[17] J. A. Johannessen *et al.*, "Direct ocean surface velocity measurements from space: Improved quantitative interpretation of Envisat ASAR observations," *Geophys. Res. Lett.*, vol. 35, no. 22, p. L22608, 2008, doi: 10.1029/2008GL035709.

[18] Y. Y. Yurovsky, V. N. Kudryavtsev, S. A. Grodsky, and B. Chapron, "Ka-band dual copolarized empirical model for the sea surface radar cross section," *IEEE Trans. Geosci. Remote Sens.*, vol. 55, no. 3, pp. 1629–1647, Mar. 2017.

[19] V. N. Kudryavtsev, B. Chapron, A. G. Myasoedov, F. Collard, and J. A. Johannessen, "On dual co-polarized SAR measurements of the ocean surface," *IEEE Geosci. Remote Sens. Lett.*, vol. 10, no. 4, pp. 761–765, Jul. 2013.

[20] C. W. Fairall, E. F. Bradley, J. E. Hare, A. A. Grachev, and J. B. Edson, "Bulk parameterization of air–sea fluxes: Updates and verification for the COARE algorithm," *J. Clim.*, vol. 16, pp. 571–591, Feb. 2003.

[21] D. Johnson, "DIWASP, a directional wave spectra toolbox for MATLAB: User manual," Centre Water Res., Univ. Western Australia, Crawley, WA, Australia, Res. Rep. WP-1601-DJ (V1.1), 2002.

[22] A. T. Jessup, W. K. Melville, and W. C. Keller, "Breaking waves affecting microwave backscatter: 1. Detection and verification," *J. Geophys. Res. Oceans*, vol. 96, no. C11, pp. 20547–20559, 1991.

[23] W. J. Plant, "The modulation transfer function: Concept and applications," in *Radar Scattering From Modulated Wind Waves*. Dordrecht, The Netherlands: Springer, 1989, pp. 155–172.

[24] P. H. Y. Lee *et al.*, "X band microwave backscattering from ocean waves," *J. Geophys. Res. Oceans*, vol. 100, no. C2, pp. 2591–2611, 1995.

[25] W. J. Plant, "A model for microwave Doppler sea return at high incidence angles: Bragg scattering from bound, tilted waves," *J. Geophys. Res. Oceans*, vol. 102, no. C9, pp. 21131–21146, 1997.

[26] Y. Liu, S. J. Frasier, and R. E. McIntosh, "Measurement and classification of low-grazing-angle radar sea spikes," *IEEE Trans. Antennas Propag.*, vol. 46, no. 1, pp. 27–40, Jan. 1998.

[27] J. Seemann, M. Stresser, F. Ziemer, J. Horstmann, and L.-C. Wu, "Coherent microwave radar backscatter from shoaling and breaking sea surface waves," in *Proc. OCEANS*, Taipei, Taiwan, Apr. 2014, pp. 1–5.

[28] T. Lamont-Smith, T. Waseda, and C. K. Rheem, "Measurements of the Doppler spectra of breaking waves," *IET Radar, Sonar Navigat.*, vol. 1, no. 2, pp. 149–157, Apr. 2007.

[29] A. T. Jessup, W. K. Melville, and W. C. Keller, "Breaking waves affecting microwave backscatter: 2. Dependence on wind and wave conditions," *J. Geophys. Res. Oceans*, vol. 96, no. C11, pp. 20561–20569, 1991.

[30] M. J. Smith, E. M. Poulter, and J. A. McGregor, "Doppler radar measurements of wave groups and breaking waves," *J. Geophys. Res. Oceans*, vol. 101, no. C6, pp. 14269–14282, 1996.

[31] O. M. Phillips, "Spectral and statistical properties of the equilibrium range in wind-generated gravity waves," *J. Fluid Mech.*, vol. 156, pp. 505–531, Jul. 1985.

[32] V. A. Dulov, V. Kudryavtsev, and A. N. Bolshakov, "A field study of white caps coverage and its modulations by energy containing waves," in *Gas Transfer at Water Surface*, M. A. Donelan, W. M. Drennan, E. S. Saltzman, and R. Wanninkhof, Eds. Washington, DC, USA: AGU, 2002, pp. 187–192.

[33] W. J. Plant, "Whitecaps in deep water," *Geophys. Res. Lett.*, vol. 39, no. 16, p. L16601, 2012, doi: 10.1029/2012GL052732.

[34] M. W. Hansen *et al.*, "Simulation of radar backscatter and Doppler shifts of wave-current interaction in the presence of strong tidal current," *Remote Sens. Environ.*, vol. 120, pp. 113–122, May 2012.

[35] V. Kudryavtsev and B. Chapron, "On growth rate of wind waves: Impact of short-scale breaking modulations," *J. Phys. Oceanogr.*, vol. 46, no. 1, pp. 349–360, 2016.

[36] V. Kudryavtsev, M. Yurovskaya, B. Chapron, F. Collard, and C. Donlon, "Sun glitter imagery of ocean surface waves. Part 1: Directional spectrum retrieval and validation," *J. Geophys. Res. Oceans*, vol. 122, no. 2, pp. 1369–1383, 2017.

[37] V. Kudryavtsev, M. Yurovskaya, B. Chapron, F. Collard, and C. Donlon, "Sun glitter imagery of surface waves. Part 2: Waves transformation on ocean currents," *J. Geophys. Res. Oceans*, vol. 122, no. 2, pp. 1384–1399, 2017.

[38] Y. Y. Yurovsky, V. Kudryavtsev, and B. Chapron, "Simultaneous radar and video observations of the sea surface in field conditions," in *Proc. Prog. Electromagn. Res. Symp.*, Saint Petersburg, Russia, May 2017, pp. 1–8.

[39] M. V. Yurovskaya, V. A. Dulov, B. Chapron, and V. N. Kudryavtsev, "Directional short wind wave spectra derived from the sea surface photography," *J. Geophys. Res. Oceans*, vol. 118, no. 9, pp. 4380–4394, 2013.

[40] V. Kudryavtsev, I. Kozlov, B. Chapron, and J. A. Johannessen, "Quad-polarization SAR features of ocean currents," *J. Geophys. Res. Oceans*, vol. 119, no. 9, pp. 6046–6065, 2014.

[41] V. Kudryavtsev, D. Hauser, G. Caudal, and B. Chapron, "A semiempirical model of the normalized radar cross-section of the sea surface 1. Background model," *J. Geophys. Res. Oceans*, vol. 108, no. C3, p. C08054, 2003, doi: 10.1029/2001JC001003.

[42] V. Kudryavtsev, A. Myasoedov, B. Chapron, J. A. Johannessen, and F. Collard, "Imaging mesoscale upper ocean dynamics using synthetic aperture radar and optical data," *J. Geophys. Res. Oceans*, vol. 117, no. C4, p. C04029, 2012, doi: 10.1029/2011JC007492.

[43] N. Rascle, F. Nouguier, B. Chapron, A. Mouche, and A. Ponte, "Surface roughness changes by finescale current gradients: Properties at multiple azimuth view angles," *J. Phys. Oceanogr.*, vol. 46, no. 12, pp. 3681–3694, 2016.

[44] Y. Wang, H. Li, Y. Zhang, and L. Guo, "The measurement of sea surface profile with X-band coherent marine radar," *Acta Oceanologica Sin.*, vol. 34, no. 9, pp. 65–70, 2015, doi: 10.1007/s13131-015-0731-7.

[45] F. G. Bass, I. M. Fuks, A. I. Kalmykov, I. E. Ostrovsky, and A. D. Rosenberg, "Very high frequency radiowave scattering by a disturbed sea surface—Part I: Scattering from a slightly disturbed boundary," *IEEE Trans. Antennas Propag.*, vol. 16, no. 5, pp. 554–559, Sep. 1968.

[46] J. Wright, "A new model for sea clutter," *IEEE Trans. Antennas Propag.*, vol. 16, no. 2, pp. 217–223, Mar. 1968.

[47] F. T. Ulaby, R. K. Moore, and A. K. Fung, *Microwave Remote Sensing: Active and Passive*, vol. 3. Dedham, MA, USA: Artech House, 1986, pp. 1065–2126.

Yury Yu. Yurovsky was born in Yalta, Russia, in 1984. He received the M.S. degree in geophysics from the Black Sea Branch, Moscow State University, Sevastopol, Russia, in 2006, and the Ph.D. degree in marine physics from the Marine Hydrophysical Institute (MHI), Sevastopol, in 2012.

Since 2007, he has been with MHI, where he currently holds a researcher position with participating in activities at the Black Sea research platform. His research mainly includes obtaining and analysis of the data in various field experiments. His research interests include ocean radar and optical remote sensing, sea surface dynamics, and air–sea interaction.

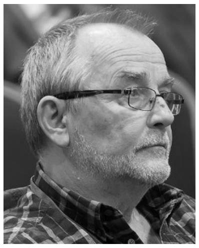

Vladimir N. Kudryavtsev received the Ph.D. and Senior Doctorate degrees in geophysics/marine physics from the Marine Hydrophysical Institute (MHI), Sevastopol, Russia, in 1981 and 1991, respectively.

In 1976, he joined MHI, where he is currently a part-time Principal Scientist. Since 2002, he has been a Professor with Russian State Hydrometeorological University, Saint Petersburg, Russia, where he is also the Head of the Satellite Oceanography Laboratory. From 2005 to 2013, he was with the Nansen Centre, Saint Petersburg. Until 2016, he held a part-time senior position with the Nansen Centre, Bergen, Norway. His research interests include air–sea interaction, atmospheric and oceanic boundary layers, and radar and optical imaging of the ocean surface.

Bertrand Chapron was born in Paris, France, in 1962. He received the B.Eng. degree from the Institut National Polytechnique de Grenoble, Grenoble, France, in 1984, and the Doctorat National (Ph.D.) degree in fluid mechanics from the University of Aix-Marseille II, Marseille, France, in 1988.

He was a Post-Doctoral Research Associate with the NASA/GSFC/Wallops Flight Facility, Wallops Island, VA, USA, for three years. He has experience in applied mathematics, physical oceanography, electromagnetic waves theory, and its application to ocean remote sensing. He is currently responsible for the oceanography with the Space Laboratory, Institut Français de Recherche pour l'Exploitation de la Mer, Plouzané, France.

Semyon A. Grodsky received the Ph.D. degree in geophysics from the Marine Hydrophysical Institute (MHI), Sevastopol, Russia, in 1986.

He was with MHI in 1999. He joined the Atmospheric and Oceanic Science Department, University of Maryland at College Park, College Park, MD, USA, where he is currently a Research Scientist. His research interests include satellite remote sensing, air–sea interactions, and various aspects of ocean data analysis.